JOURNAL OF GEOPHYSICAL RESEARCH, VOL. 104, NO. C12, PAGES 29,613–29,635, DECEMBER 15, 1999

An analysis of tropical instability waves in a numerical model of the Pacific Ocean
1. Spatial variability of the waves

S. Masina[1] and S.G.H. Philander

Atmospheric and Oceanic Sciences Program, Princeton University, Princeton, New Jersey

Abstract. Unstable oscillations confined within the mixed layer close to the equator are generated in wind-forced experiments performed in a multilevel general circulation model configured for the tropical Pacific Ocean. The experiments indicate that the waves develop preferentially in the eastern Pacific along the northern temperature front. However, there is clear evidence of a second unstable region along the southern temperature front in the central Pacific. In both regions the instabilities propagate westward, but in the central Pacific their phase speed is considerably smaller. The differences between the wave characteristics in the eastern and central Pacific are closely correlated to the differences in the time mean conditions of the flow. The eastern instabilities have a structure with two peaks in amplitude: one located on the equator and the other a few degrees north of it. Their dispersion characteristics show many similarities to those of tropical instability waves (TIWs) observed in the Pacific Ocean, while the instabilities which grow in the central Pacific do not have any known observed correspondents. We explore the spatial variability of the simulated waves through a wavelet analysis, which provides detailed results on how the period and wavelength of the instabilities change as a function of longitude, latitude, and depth. The wavelet analysis reveals that in the eastern Pacific and close to the surface the TIWs have a phase speed of -48 cm/s, while in the central Pacific they have a phase speed of -11 cm/s. In particular, the change in the phase speed is due to a change in the dominant period of the TIWs: The period of the central Pacific instabilities is considerably longer than the period of the instabilities present in the eastern Pacific.

1. Introduction

Motivated by the data that have been collected in the Atlantic and Pacific Oceans on TIWs [e.g., *Legeckis*, 1977; *Weisberg*, 1979], several attempts have been made to simulate TIWs with a hierarchy of numerical models of varying complexity. *Philander* [1976] used 1.5- and 2.5-layer models to investigate the effects of β and divergence on the stability of zonal currents in the tropical oceans. He found that with a highly idealized profile of the equatorial zonal currents, which included a strong South Equatorial Current (SEC) and Equatorial Undercurrent (EUC), the most unstable wave propagated westward with a period of 16 days and a wavelength of 2000 km. In a subsequent paper, *Philander* [1978a] used the 1.5-layer model to study the stability of a meridional profile of the surface currents in the equatorial Atlantic and Pacific Oceans that resembled the northern branch of the SEC and the North Equatorial Countercurrent (NECC). In this case the stability analysis revealed that the most unstable waves are westward propagating and have a period of $\sim$ 1 month, a wavelength of $\sim$ 1100 km, and an e-folding time near 2 weeks.

Cox [1980] used a multilevel general circulation model configured for the equatorial Pacific Ocean and driven by monthly varying winds. The flow becomes unstable north of the equator in the boreal fall on the edge of the cold tongue and generates waves with a 1000 km wavelength and a period of 1.1 months. This instability persists into boreal winter, when the southern branch of the SEC reaches its maximum speed in the central and west central Pacific. During boreal winter the SEC can become unstable and develop disturbances that are similar to but weaker than the oscillations generated in the eastern Pacific during boreal fall. This boreal winter disturbance is shorter lived and reaches its maximum amplitude in March. There is some additional evidence for the presence of different kinds of linear planetary waves that are excited by the instability. These waves

[1]Now at Istituto di Scienze dell'Atmosfera e dell'Oceano, CNR, Bologna, Italy.

Paper number 1999JC900227.
0148-0227/99/1999JC900227$09.00

are shown to carry energy away from the generation area, which is confined to the upper ocean near the equator.

Seigel [1985] used the channel model of *Cox* [1980] to show how the period of the unstable oscillations in the Pacific Ocean depends on the strength of the SEC. The maximum speed of the westward current is more important than the horizontal shear between the SEC and the EUC in determining the period of the waves. The more intense the SEC, the faster the phase speed of the instability and the shorter the period of the waves. The wavelength of the most unstable waves is shown not to be dependent on the intensity of the SEC, a result that confirms that of *Philander* [1978a], who demonstrated that it is the horizontal scale of the shear and not the magnitude of the currents that determines the wavelength. In a recent study, *Proehl* [1996] suggested that the instabilities that develop in equatorial flows with oceanic scales are associated with the presence of critical layers. In this case the dispersion and growth characteristics of the most unstable wave are determined only by the location of the reflection surfaces as prescribed by the overreflection theory.

Semtner and Holland [1980] forced a primitive equation model with a constant (in space and in time) 0.5 dyn/cm^2 wind stress. The induced currents are unstable and develop westward propagating waves a few degrees both north and south of the equator. These waves have a period of 33 days and a wavelength of 800 km. They are symmetric about the equator and decay as they propagate westward from the generation region. Their structure seems to be very similar to that of equatorially trapped first meridional and first baroclinic Rossby waves. In the observations, however, these types of waves appear preferentially north of the equator. The discrepancy of this numerical solution with the observed data must be due to the horizontally uniform wind stress that was applied. Under such conditions the model is also unable to simulate the NECC. Interestingly, however, this simulation shows that the presence of the NECC is not crucial for the development of instability waves in the equatorial region.

Schopf and Cane [1983] used a model that combines primitive equation dynamics with a parameterization of mixed layer physics in order to study the interaction between hydrodynamics and thermodynamics in the equatorial ocean. They showed that a sharp discontinuity in mixed layer depth forms between the upwelling region at the equator and the downwelling region at a more poleward latitude. The meridional temperature advection is enhanced on the shallow, cold side of the discontinuity and, as a result, a temperature front is created. This front eventually becomes unstable and breaks down into a series of regular eddies centered at 4°-5° latitude both north and south of the equator. These waves have a wavelength of 800 km and look very similar to those found by *Semtner and Holland* [1980] in their simulations, despite the fact that considerably different physics are involved in the two studies of *Schopf and Cane* [1983] and *Semtner and Holland* [1980].

Waves with a period of the order of 1 month and a wavelength of the order of 1000 km have been observed by *Philander et al.,* [1986] in general circulation models that realistically simulate the seasonal cycle of the tropical Atlantic and Pacific Oceans. In the study of *Philander et al.,* [1986] it was demonstrated that the seasonal and longitudinal changes in the shear of the currents affect the amplitude, period, and wavelength of the waves. The waves are absent during the boreal spring and early summer and are also absent from the eastern Atlantic and far western Pacific.

McCreary and Yu [1992] studied the generation of mean flow instabilities in a 2.5-layer model. The model allows for an exchange of water between the two active layers, and as a consequence, the temperature of these two layers can vary. All solutions are forced by an idealized representation of the Pacific trade winds which contains no latitudinal dependence. Consequently, the mean flow does not include the NECC, and the instabilities that develop have a meridional flow field which is either symmetric (same sign) or antisymmetric (opposite sign) about the equator with the same amplitude (in modulus) north and south. Three kinds of unstable oscillations are excited in the model: a symmetric oscillation with a period and a wavelength of $\sim$ 28 days and 1100 km that resembles a first meridional Rossby wave, an upper layer antisymmetric disturbance with a period of $\sim$ 21 days, and a lower layer antisymmetric instability at lower frequencies (from 35 to 53 days) that causes a meandering of the EUC. None of these oscillations show any meridional asymmetry, but if the background SEC is made asymmetric about the equator with a weaker southern branch, then the unstable waves become prominent north of the equator [*Yu et al.,* 1995].

It is clear that both simple homogeneous layer models and complex continuously stratified general circulation models (GCMs) are potentially capable of generating unstable waves that as in the observations, vary considerably in terms of their basic characteristics such as wavelength and period. However, so far, none of these numerical studies have tried to analyze the complex three-dimensional structure of the waves and their spatial dependence in detail. The complexity of, and sometimes the discrepancy between, the model results clouds the explanation for the dependence of the tropical instability waves (TIWs) on the mean flow circulation and especially their high inhomogeneity in space.

In order to accomplish this, numerical experiments have been performed in a multilevel general circulation model configured for the equatorial Pacific Ocean and forced with steady wind stress. The wind forcing applied to the model is chosen in order to reproduce a strong La Niña condition, i.e., the most favorable oceanic conditions for the development of TIWs as suggested by observations. Our main goals are to

reproduce mean flow instability waves that are similar to the Legeckis waves observed in the Pacific Ocean and to examine their three-dimensional spatial variability. In particular, a wavelet analysis of the simulated data provided detailed results on how the period and wavelength of the instabilities change as a function of longitude, latitude, and depth.

A brief description of the model, the initial condition, and the forcing applied is given in section 2. In section 3 we describe in detail the results from the numerical simulations. A discussion of the zonal and meridional variability of the instabilities with emphasis on a comparison between the eastern and central Pacific instabilities and how they are correlated to the differences in the mean conditions is included. The results of a wavelet analysis of the instabilities and a short description of the method are presented in section 4. Finally, we summarize and conclude in section 5.

2. Numerical Model: Model Setup and Forcing

The model used for these simulations is the Modular Ocean Model (MOM) [*Pacanowski et al.,* 1993] produced at the Geophysical Fluid Dynamics Laboratory (GFDL). This model is based on the primitive equation numerical ocean model originally developed by *Bryan and Cox* [1967] and described in detail by *Cox* [1984].

The domain that we have chosen is the portion of the Pacific Ocean confined between 134°E and 96°W and between 30°S and 30°N. The domain does not include the far eastern Pacific; this choice, made for computational reasons, is justified by *Cox's* [1980] results, which demonstrate that the equatorial region east of 110°W is stable. The model resolution is 1° in longitude and is variable in latitude, with 1/3° resolution within 10° of the equator that increases poleward to 1° between 10° and 30°. The finest resolution in the equatorial zone allows us to better resolve the spatial structure of the TIWs. Eighteen vertical levels are unevenly spaced in a flat bottom basin. There are 10 levels in the top 100 m to better resolve the thermocline, after which the level thickness increases with depth down to the bottom at 3000 m. This choice of grid resolution is consistent with the aspect ratio of the expected frontal zones; namely,

$$\Delta z \sim \frac{f}{N}\Delta y, \tag{1}$$

in which Δz and Δy are the vertical and meridional grid scales. Here f/N is a geostrophic estimate for the slope of the front induced by the growth of baroclinic waves [*Orlanski,* 1986]. It has been shown that such an estimate can also be extended to the nongeostrophic regime [*Orlanski and Cox,* 1973], and for this reason it is applicable to our case. Using typical equatorial values for f and N ($\sim 10^{-2}$/s), this aspect ratio argument still applies using our resolution, and therefore we anticipate adequate resolution to capture the physics of instabilities in equatorial frontal zones. The time step for advective and diffusive calculations is 1 hour. A "sponge" condition is applied at the northern and southern lateral boundaries; it strongly increases the horizontal mixing of momentum over the four outermost rows of the numerical grid as the boundaries are approached. This sponge layer is applied to avoid wave reflection at the artificial walls that would bring energy back into the basin. The horizontal and vertical mixing schemes and the use of Newtonian damping and sponge boundaries at the lateral walls are typical for equatorial numerical simulations [*Philander and Pacanowski,* 1986; *Philander et al.,* 1987]. Since TIWs are strongly equatorially trapped, we choose the meridional scale of the domain to be large enough to ensure that they are not affected by the sponge boundaries. The coefficient of horizontal viscosity has a minimum value of 2.0 x $10^7 \mathrm{cm}^2/\mathrm{s}$ in the active domain, and it linearly increases 1 order of magnitude inside the sponge layer. The horizontal diffusivity is kept constant at 2.0 x $10^7 \mathrm{cm}^2/\mathrm{s}$.

In the vertical direction the *Pacanowski and Philander* [1981] vertical mixing scheme is used for both tracers and momentum. This Richardson number-dependent vertical scheme is designed primarily for equatorial models. In regions of potential gravitational instability, the density profile is altered using a large vertical mixing coefficient to regain a gravitationally stable stratification.

The momentum flux at the surface is given by a wind stress, which is based on the bulk aerodynamic formula with the magnitude of the surface wind vectors taken relative to the velocity of the ocean surface [*Pacanowski,* 1987]. This formulation is especially required in the equatorial region where the surface currents can exceed speeds of 1 m/s.

The heat flux across the ocean surface and the equations for sensible and latent heat flux at the surface are described by *Philander et al.,* [1987]. Both the salinity and the temperature fields are restored at the northern and southern walls of the domain to *Levitus* [1982] August climatology with a latitude-dependent damping timescale that decreases from 120 to 30 days over the outermost four meridional gridpoints near the boundaries.

The initial condition and the forcing that we have chosen are both intended to reproduce a strong La Niña condition. The model was initialized with a temperature and salinity distribution given by the *Levitus* [1982] August climatology. Current velocities are initially zero. In order to spin up the model we apply surface wind stress and thermal forcing from the Comprehensive Ocean Atmosphere Data Set (COADS). With respect to climatology the trade winds in the equatorial region during the boreal summer of 1988 are intensified. In particular, the wind stress consists of an August climatological mean component plus the August 1988 monthly mean perturbation component. Air

temperature, cloudiness, and surface winds for the 1988 August condition are applied to the model and do not vary with time.

3. Results

Two model experiments have been integrated forward in time for 3 years with the only difference between them being the wind stress forcing. In the first experiment the monthly mean wind stress from COADS data for August 1988 has been applied, while in the second experiment the same wind stress pattern is applied, but its amplitude has been reduced to 65% of its original value in order to represent the wind relaxation at the end of the La Niña event. Waves with characteristics similar to the observed unstable waves in the Pacific Ocean are generated by the model in both experiments. Their amplitude is not significantly affected by the strength of the wind stress, and therefore we present only results from one of the two experiments; namely, we show the experiment forced with weaker winds.

All the time mean fields have been obtained through averaging the last 360 days of the third year of integration of the numerical model. We decided to average over this period because after 2 years of integration, the transients associated with the spin-up have definitely vanished and the dynamical fields have reached a quasi-steady state.

In Figure 1a we show the time mean temperature and zonal velocity at z=5 m. At this depth the time mean zonal circulation is characterized by a SEC with a maximum speed of 60 cm/s and is confined between 2°S and 5°N at all longitudes in the model domain. North of 5°N the NECC is clearly visible, and its maximum velocity is 20 cm/s. The time mean temperature minimum (22°C) is found farther east in the Pacific on the equator. The temperature cold tongue in the equatorial region is a consequence of upwelling of cold water in this region. The zonal component of the wind stress at the equator induces an Ekman divergent flow, which in turn, produces upwelling. In the eastern equatorial Pacific the winds are predominantly northward, and therefore they produce a strong divergence zone south of the equator and a narrow convergence zone north of the equator. This explains why the strongest temperature front occurs in the eastern Pacific (100°- 110°W) between 1° and 3°N. The meridional temperature gradient along the northern front decreases going westward. On the contrary, the temperature front that develops south of the equator is weaker and more diffuse than the northern front in the eastern Pacific but becomes stronger going westward. From 130° to 160°W the southern front is centered at 1°S and is clearly stronger than the northern front at the same longitude.

In Figure 1b we show a snapshot of temperature and velocity vectors in the upper level of the model in the eastern Pacific taken after $\sim$ 2 years of integration. The presence of eddies at the ocean surface is readily detected in the patterns of surface temperature because of the presence of strong wavelike temperature fronts on either side of the equator. The surface oscillations develop with preference north of the equator in the eastern Pacific. Some eddies also develop south of the equator, but their signal is less prominent, and their meridional extent is considerably smaller than that of the eddies to the north of the equator. The motion is convergent in the cold crest of the waves, where there is downwelling, while it is divergent in the warm troughs, where there is upwelling [see also *Philander et al.,* 1986].

The vertical scale of the fluctuations associated with these waves is confined to the region above the thermocline. This means that the wave signal never extends deeper than the upper 100-200 m, which is the thermocline depth.

In Figures 2a and 2b we show the Hovmöller diagrams of the perturbation meridional velocity V' (hereafter the perturbation quantities refer to the total quantities minus the time average) at a depth of 95 m at two different latitudes: 2°S and 2°N, respectively. Evident from Figure 2 is that westward propagating fluctuations are present both north and south of the equator. These waves are generated in the eastern Pacific and reach their maximum amplitude between 120° and 140°W, beyond which they decay.

Two distinct and zonally separated wave regions are clearly visible south of the equator (Figure 2a). At 2°S the phase velocity of the wave signal decreases considerably from approximately -50 cm/s east of 160°W to approximately -10 cm/s west of 160°W, and the amplitude of the waves in the central region of the domain is comparable to that of the waves in the eastern region. On the contrary, at 2°N the phase velocity is constant over the whole domain at approximately -50 cm/s, and the oscillations are much more intense in the eastern region. The wave signal north of the equator gradually and constantly weakens during its westward propagation. At 170°W north of the equator the perturbation amplitude is 4 times weaker than at 130°W.

3.1. Eastern Pacific Instability

In order to explore the reasons that cause the dramatic change in the wave signal between the eastern and central regions of the domain south of the equator we first examine how the time mean and perturbation fields change in longitude. In Figure 3a the time mean zonal velocity (shaded) is shown as a function of latitude and depth at 130°W. The contour plot in Figure 3a is a snapshot of the perturbation meridional velocity. The EUC maximum speed is 90 cm/s at 90 m. The SEC reaches a maximum westward speed of 60 cm/s. The maximum velocity in the SEC is attained at the surface. The core of the EUC is located south of the equator because of the south-north component of the wind stress in the eastern Pacific. The strongest mean flow meridional shears occur between the EUC and the SEC between the equator and 2°N and in the EUC itself

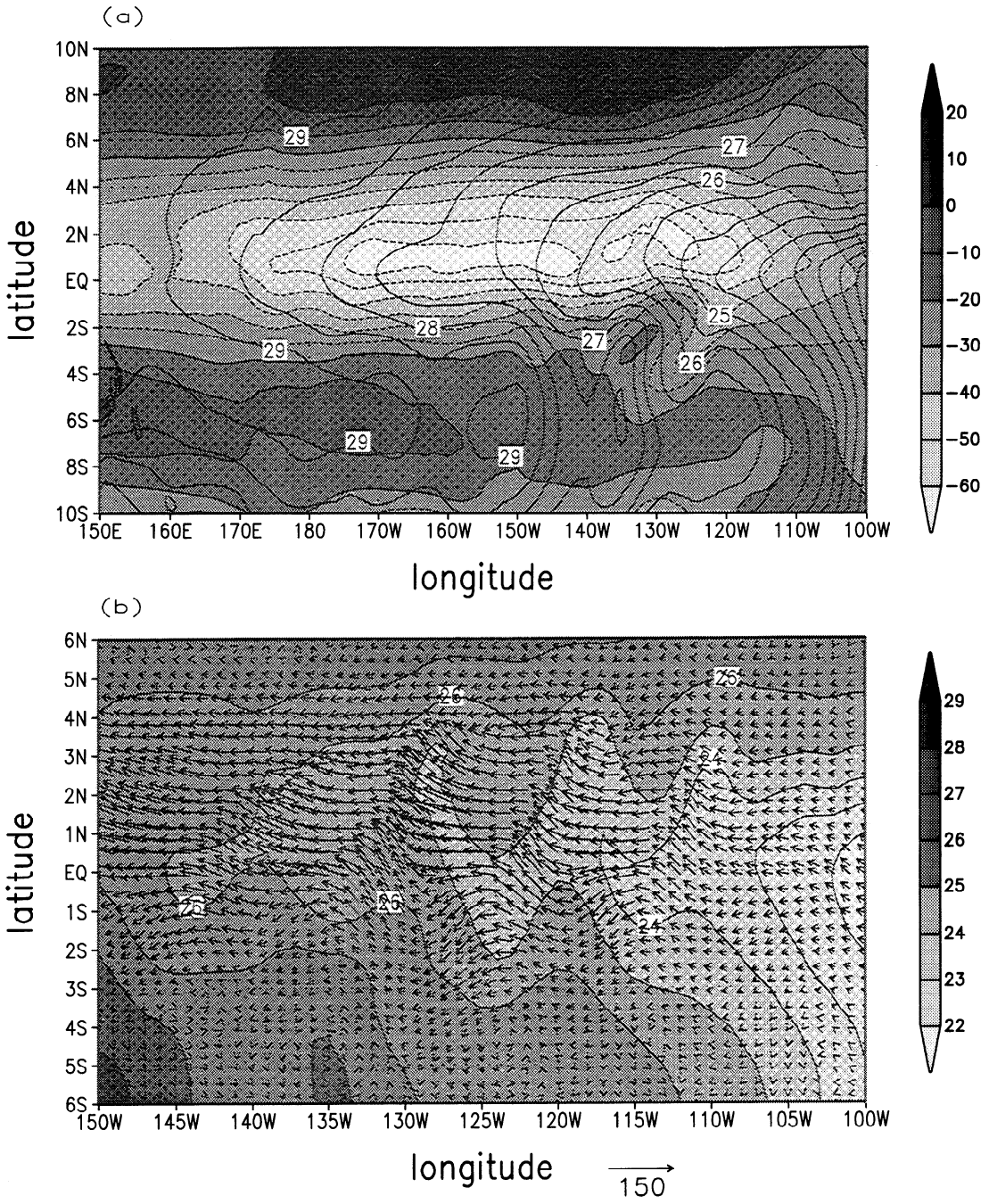

Figure 1. (a) Horizontal section of time mean zonal velocity U (shaded) and temperature T (contour) at 5 m. Contour intervals (CI) are 0.5°C for temperature and 10 cm/s for velocity. (b) Snapshot of temperature (shaded) and horizontal current (vectors) at 5 m. Contour intervals are 1°C for temperature, and the unit vector is 150 cm/s.

at 2°S. In these two regions the perturbation meridional velocity reaches two maxima in amplitude. The shear between the EUC and the SEC is barotropically unstable as shown by *Masina et al.* [this issue].

The meridional shear between the northern branch of the SEC and the NECC is much weaker than the shear between the SEC and the EUC, supporting the conclusion that the NECC does not significantly affect the generation of unstable waves in the Pacific Ocean [*Yu et al.*, 1995]. In our simulation the NECC develops poleward of 6°N and reaches a maximum speed of 20 cm/s.

In Figure 4a the same snapshot of the perturbation meridional velocity shown in Figure 3a is superimposed on the time mean temperature field at 130°W. As is evident from Figure 4a, the mixed layer is deeper in the Northern Hemisphere, and the maximum latitudinal temperature gradient exists at 4°N where another

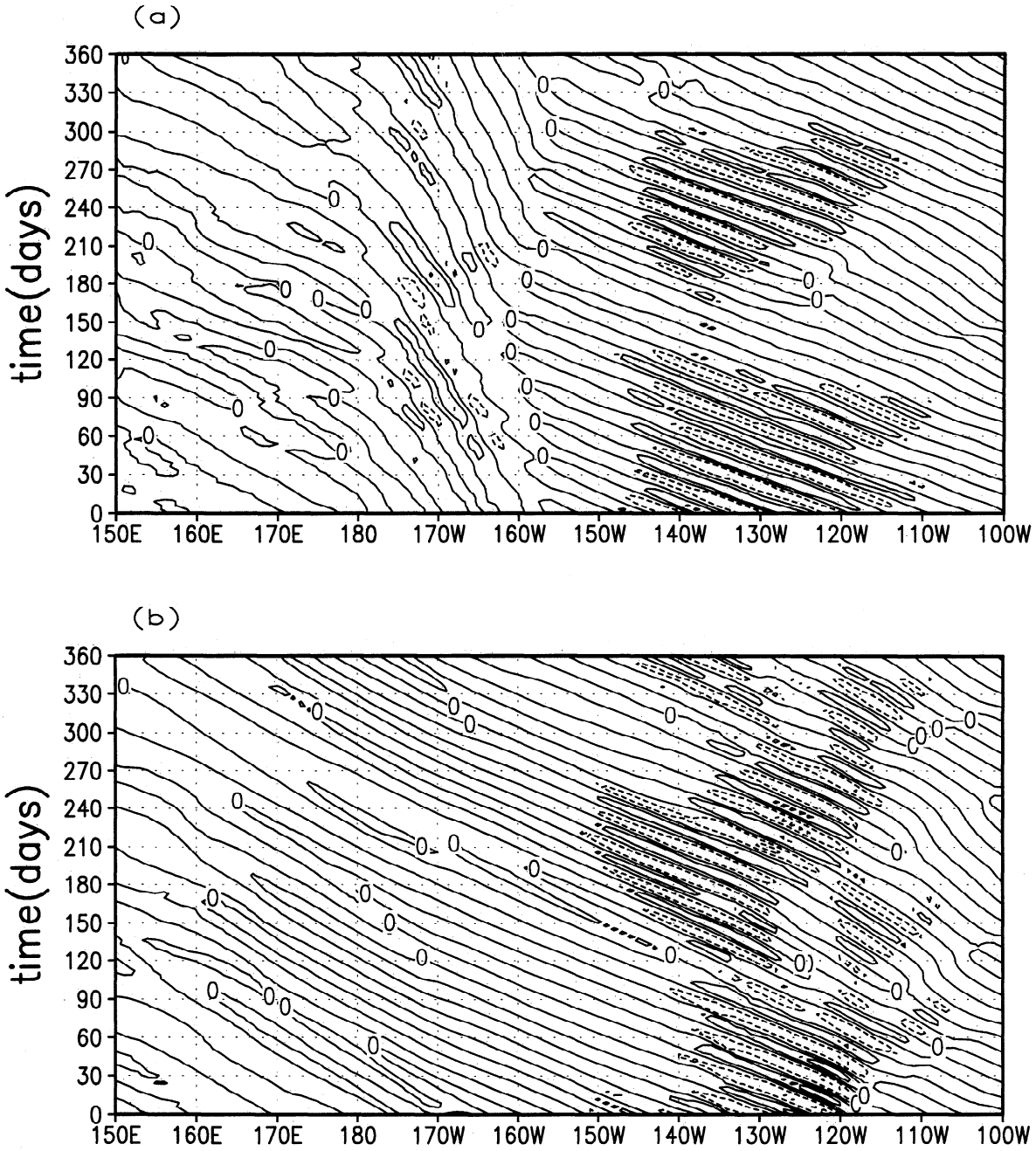

Figure 2. Hovmöller diagrams of perturbation meridional velocity V' at 95 m at (a) 2°S and (b) 2°N. CI is 10 cm/s in Figure 2a and 15 cm/s in Figure 2b.

maximum in the V' field is localized. This suggests that this region is the most likely candidate for baroclinic instability near the equator [*Masina et al.*, this issue]. The perturbation meridional velocity has the same vertical dependence of the mixed layer and deepens on both sides of the equator. Figure 4a shows that the instabilities are confined to the upper ocean and their vertical wavelength is comparable to the depth of the mixed layer [*Masina*, 1996].

3.2. Central Pacific Instability

As can be seen from the Hovmöller diagrams in Figures 2a and 2b, the region south of the equator between 180° and 160°W shows a sudden and drastic change in the characteristics of the oscillations with respect to the eastern and northern instabilities.

The EUC core is deeper (below 180 m) at 170°W than at 130°W, and the southern branch of the SEC is stronger and is connected to the northern branch (see Figure 3b, shaded area). At 170°W in both experiments the temperature field becomes more symmetric about the equator (Figure 4b, shaded area) and the mixed layer depth is $\simeq$ 100 m both north and south of the equator. A snapshot of the meridional velocity (contour plots in Figures 3b and 4b) shows that at this longitude the instability is mainly confined south of the equator.

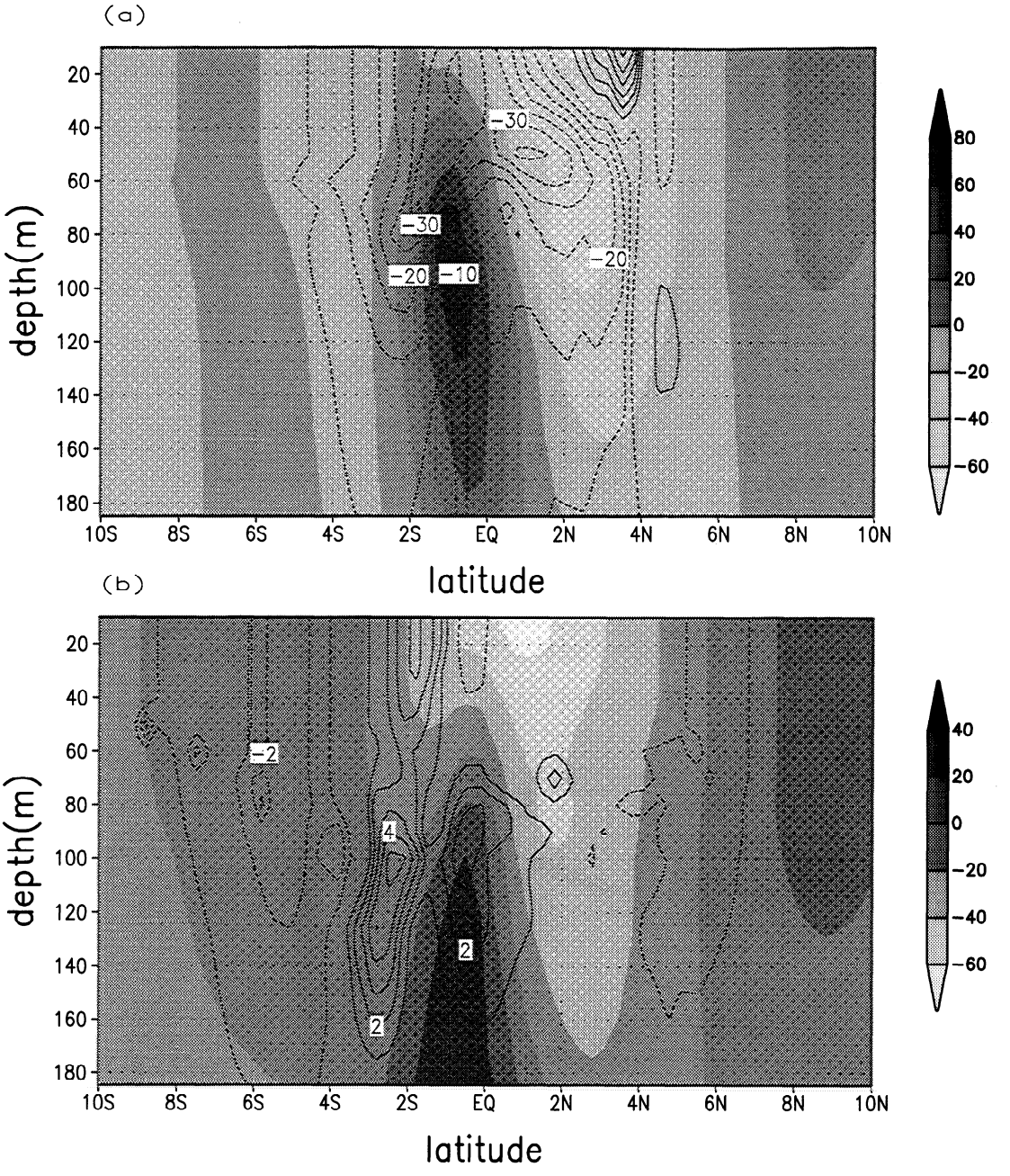

Figure 3. Depth-latitude sections of time mean zonal velocity (shaded) and instantaneous perturbation meridional velocity (contour) at (a) 130°W and (b) 170°W. CI is 20 cm/s in both plots for zonal velocity and, for meridional velocity, is 10 cm/s in Figure 3a and 1 cm/s in Figure 3b.

The vertical structure of the instability is deeper than in the eastern Pacific, confirming that the oscillations are confined in the mixed layer. The maxima in amplitude of the V' field are localized in the southern branch of the SEC.

In summary, the structure of the temperature field is more symmetric about the equator in the central Pacific than in the eastern Pacific. The structure and the amplitude of the time mean zonal flow change considerably south of the equator between the eastern and the central domain. In the central region the meridional shear of the zonal currents within the mixed layer south of the equator becomes stronger because of the deepening and intensification of the southern branch of the SEC. Since the oscillations are strongly confined south of the equator in the central Pacific, we can speculate that the development of the oscillations and their drastic change in frequency in this region might be related to the development of the southern branch of the SEC.

3.3. Latitudinal Structure of TIWs

One of the most interesting features of the TIWs that is clearly seen both in observations and in our numerical simulations is their asymmetry about the equator. The oscillations grow and develop on either side of the equator but not in a symmetric way. In Figure 5 the per-

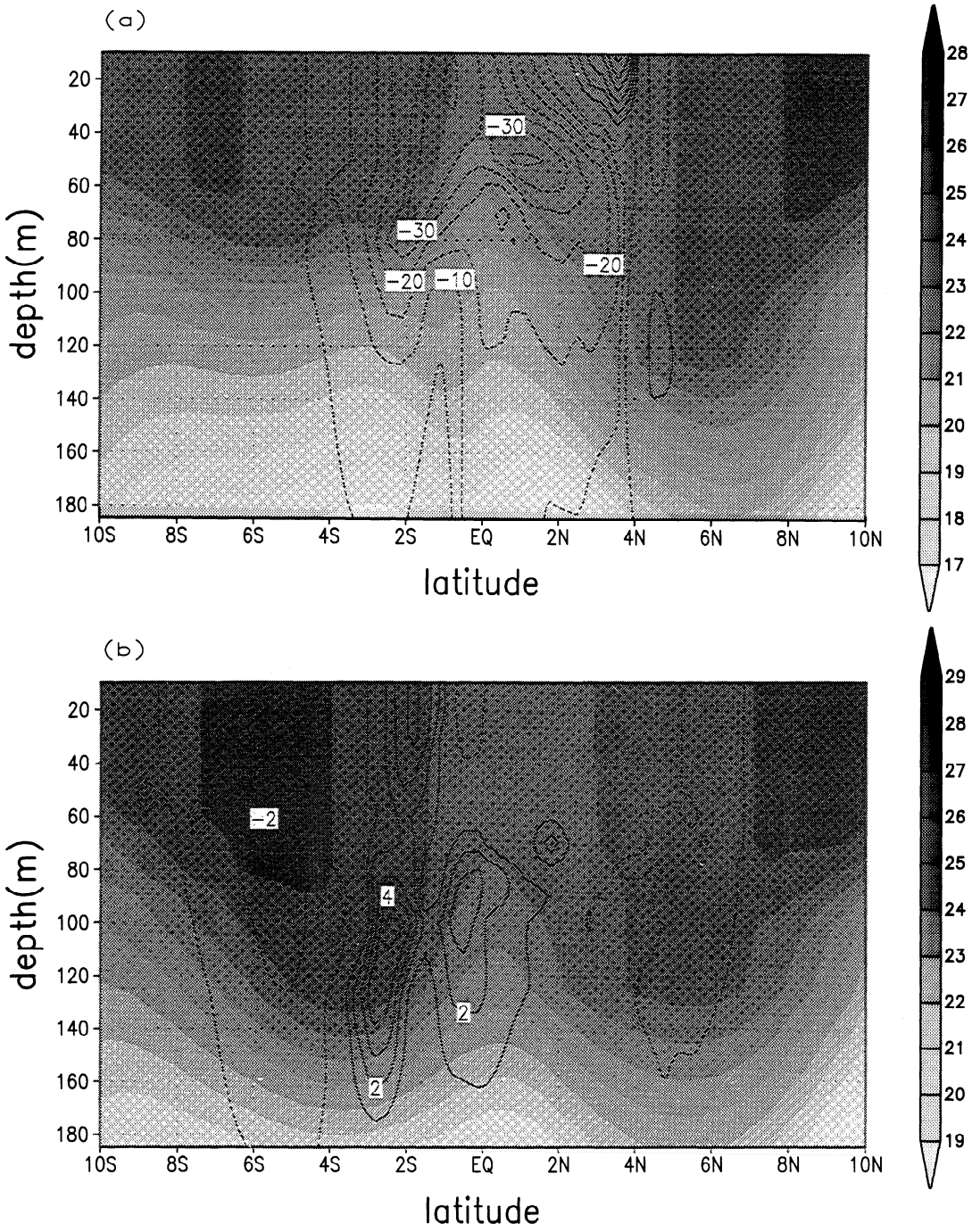

Figure 4. Depth-latitude sections of time mean temperature (shaded) and instantaneous perturbation meridional velocity (contour) at (a) 130°W and (b) 170°W. CI is 1°C in both plots for temperature and, for meridional velocity, is 10 cm/s in Figure 4a and 1 cm/s in Figure 4b.

turbation meridional velocity (contour plot) at a depth of 5 m and at 130°W shows this asymmetric behavior. The shaded plot in Figure 5 is the zonal velocity. In this time-latitude diagram it seems that the oscillations consist of two structures. One structure is localized around 3°N in the region of the SEC, and the second one grows in the boundary region between the EUC and the SEC. The two structures are phase locked and are probably part of the same instability. However, since we cannot rule out different hypotheses, we refer the reader to part 2 of this study [*Masina et al.*, this issue] for a complete discussion about this point in terms of energetic arguments.

At a lower depth (95 m; see Figure 6) the northern structure is displaced poleward, and its amplitude is comparable to the amplitude at the surface. On the contrary, the amplitude of the southern structure decreases considerably with respect to the surface. At

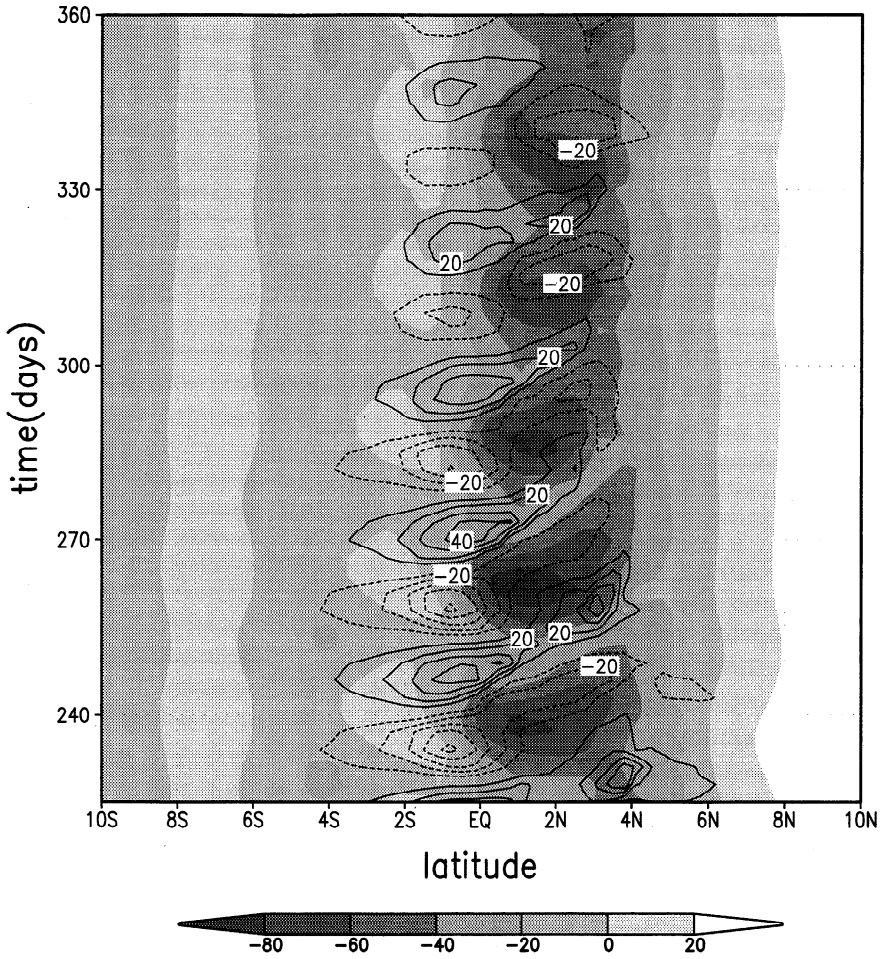

Figure 5. Time-latitude diagram of zonal velocity (shaded) and perturbation meridional velocity (contour) at 130°W and 5 m. CI is 20 cm/s for both fields.

this depth the phase shift between the two stuctures is smaller than at the surface.

A time-latitude plot of the perturbation meridional velocity superimposed on the total zonal velocity (shaded area) at 5 m and 170°W is shown in Figure 7. The perturbation meridional velocity shows very different structures north and south of the equator that have, nevertheless, approximately the same amplitude. A low-frequency wave develops south of the equator. The northern wave is still present even if much weaker than in the eastern Pacific. It develops in the northern branch of the SEC and propagates with the same phase speed as in the eastern Pacific. The southern wave has a maximum near 4°S and propagates westward and equatorward where a second maximum is centered at 1°S. The Southern Oscillation does not resemble any known linear equatorial wave structure. At 95 m below the surface at the same longitude (Figure 8), the northern signal is scattered to higher latitudes, and its amplitude is significantly weaker than that of the southern signal. On the contrary, at this depth the southern signal is more focused near the equator in the region of the EUC than it is at the surface and is stronger than at the surface.

It is possible to interpret the tilted waves south of the equator in terms of zonal momentum transport. Vertical profiles of time mean horizontal convergence of the zonal eddy momentum flux, $-(\partial\overline{(u')^2}/\partial x) - (\partial\overline{(u'v')}/\partial y)$ (where the bar means a time average and the prime the deviation from it), are shown in Figure 9b at 170°W at three different latitudes south of the equator. In Figure 9a we show the vertical profiles of time-averaged zonal velocity at the same locations. At 4°S the eddy momentum flux is divergent below 60 m, and this implies that the eddies decelerate the mean flow (which is eastward at this location). At 3°S the eddy momentum flux divergence causes a deceleration of the eastward mean flow below 65 m. Finally, at 2°S the effect of the eddies is to decelerate the flow above 60 m and accelerate it below 90 m. This means that at this latitude both the speed of the westward flow above 90 m and the speed of the eastward flow below this depth increase. In summary, considering the net effect of the eddy momentum fluxes at 170°W below 90 m, the ed-

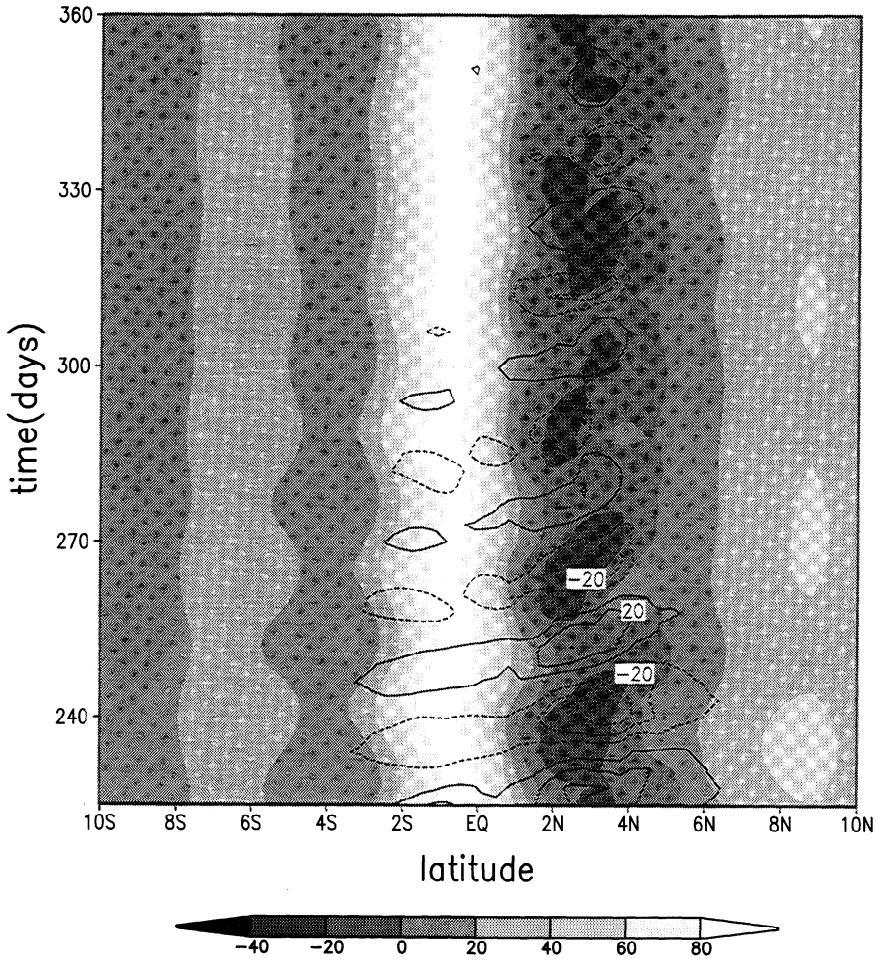

Figure 6. As in Figure 5 but at 95 m. CI is 20 cm/s for both fields.

dies transport eastward momentum equatorward, which serves to accelerate the undercurrent. On the contrary, above 40 m the net effect of the eddies is to transport westward momentum equatorward and, consequently, to accelerate the SEC.

4. Wavelet Analysis of the Numerical Simulation

We apply the wavelet transform method to the three-dimensional data set obtained from the numerical experiment described in section 3. Wavelet transforms are a relatively recent mathematical tool which allow one to unfold either a time-dependent signal into both time and frequency domains or a space-dependent signal into both space and wavenumber domains [e.g., *Farge*, 1992]. A detailed explanation and description of this method is available from *Combes et al.* [1989], as well as in the review articles by *Farge* [1992], *Meyers et al.* [1993], and *Rioul and Vetterli* [1991]. Here we will summarize the main points of this technique and give the motivations that inspired us to apply this method.

We can see the wavelet transform as a signal decomposition into a set of basis functions called wavelets. The wavelets are obtained from a single prototype wavelet, called the mother wavelet, by dilations and contractions as well as by translation.

Let $f(t)$ represent a signal that is a function of the variable t, where t can be either time or space. Its wavelet transform is defined as

$$\tilde{f}(b,a) = \frac{1}{\sqrt{a}} \int f(t)\psi^*(\frac{t-b}{a})dt, \qquad (2)$$

where $\tilde{f}(b,a)$ is the wavelet coefficient, b is the translation parameter corresponding to the time or the position of the wavelet if the data are temporal or spatial, respectively, and a ($a > 0$) is the dilation parameter that corresponds to temporal period or scale length. Both a and b are real. In this example the function $\psi(t)$ is the mother wavelet, and $\psi^*(t)$ is its complex conjugate.

A mother wavelet must satisfy the admissibility condition, which for an integrable function, means that its average should be zero. The mother wavelet must also be a function centered at $t = 0$ and in the limit as $|t| \to \infty$, $\psi(t) \to 0$ rapidly. This means that the wavelet

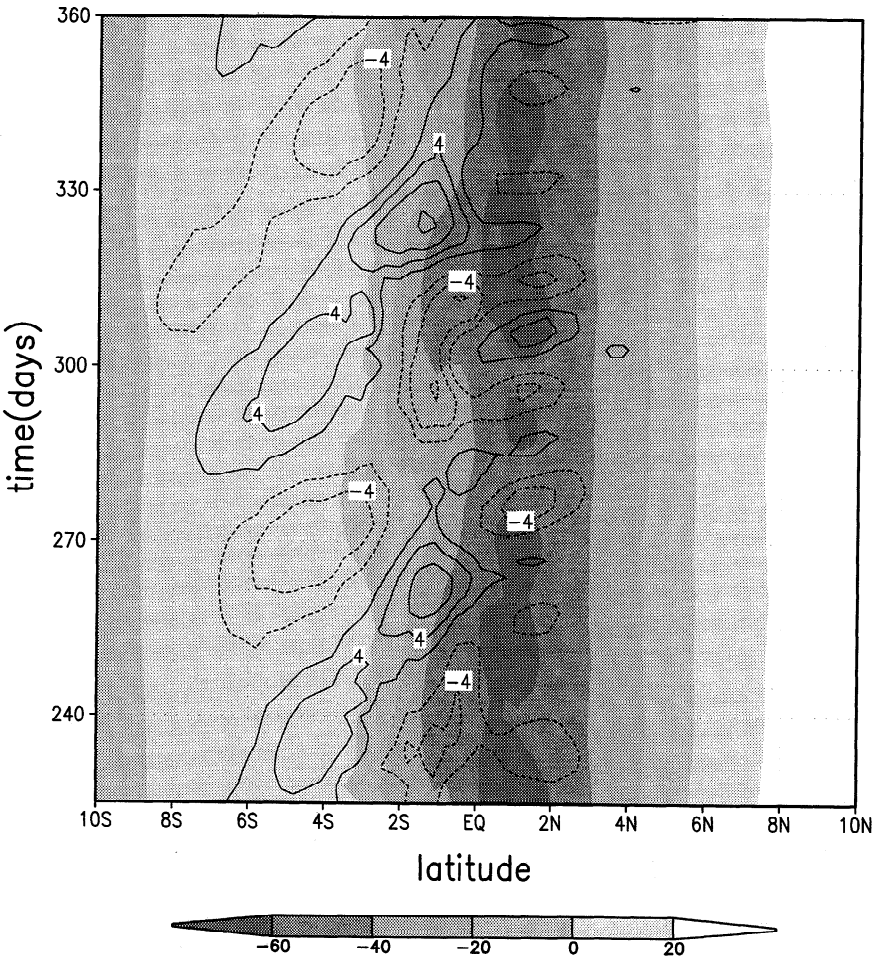

Figure 7. Time-latitude diagram of zonal velocity (shaded) and perturbation meridional velocity (contour) at 170°W and 5 m. Contour intervals are 20 cm/s for zonal velocity and 2 cm/s for meridional velocity.

is localized in time or in space, and therefore the coefficients $\tilde{f}(b,a)$ are affected only by the signal in the so-called cone of influence about $t = b$. The radius of this cone of influence is, in practice, the point in time beyond which the wavelet no longer has a significant amplitude. Usually it is proportional to a, which gives rise to the conelike structures observed in the wavelet transform. The appropriate choice of the mother wavelet depends on the aims of the analysis and the signal to be analyzed. One of the most commonly used wavelets is the Morlet wavelet, which is a plane wave of frequency ω_ψ, modulated by a Gaussian envelope. The Morlet wavelet is a complex-valued wavelet and allows one to determine amplitude (or energy) and phase of the scale a of the signal as a function of time or of space depending on the signal being a function of time or of space, respectively.

The Morlet mother wavelet that we choose to employ in this study has the form

$$\psi(t) = e^{i\omega_\psi t} e^{-|t|^2}. \tag{3}$$

We choose $|\omega_\psi| = 6$ because for smaller values the Morlet wavelet is not admissible [*Farge*, 1992]; that is, it has a mean that significantly deviates from zero, and for higher values the wavelet oscillates too rapidly, and therefore the time resolution decreases.

Constants have been chosen such that the wavelet coefficient (defined by (1)) at scale $a = 1$ gives information about a cycle with a 30 day period and at scale $a = 0.5$ gives the amplitude of a 15 day period signal. The shape of the wavelets for different values of a is such that their values decay to zero at a distance approximately equal to $2a$ from the center of the wavelet. This means that a distortion in the analyzed field occurs within regions $2a$ from the beginning and end points of the signal, and therefore results from the wavelet analysis performed in those regions are not reliable.

Since both the spatial and temporal resolutions of the numerical data are sufficient for a wavelet analysis, we analyze both temporal series at fixed longitude, latitude, and depth as well as zonal series at fixed latitude, time, and depth. This procedure will help to explain how the dominant period of the instability signal changes at different locations and how the dominant wavelength changes in the zonal direction going from

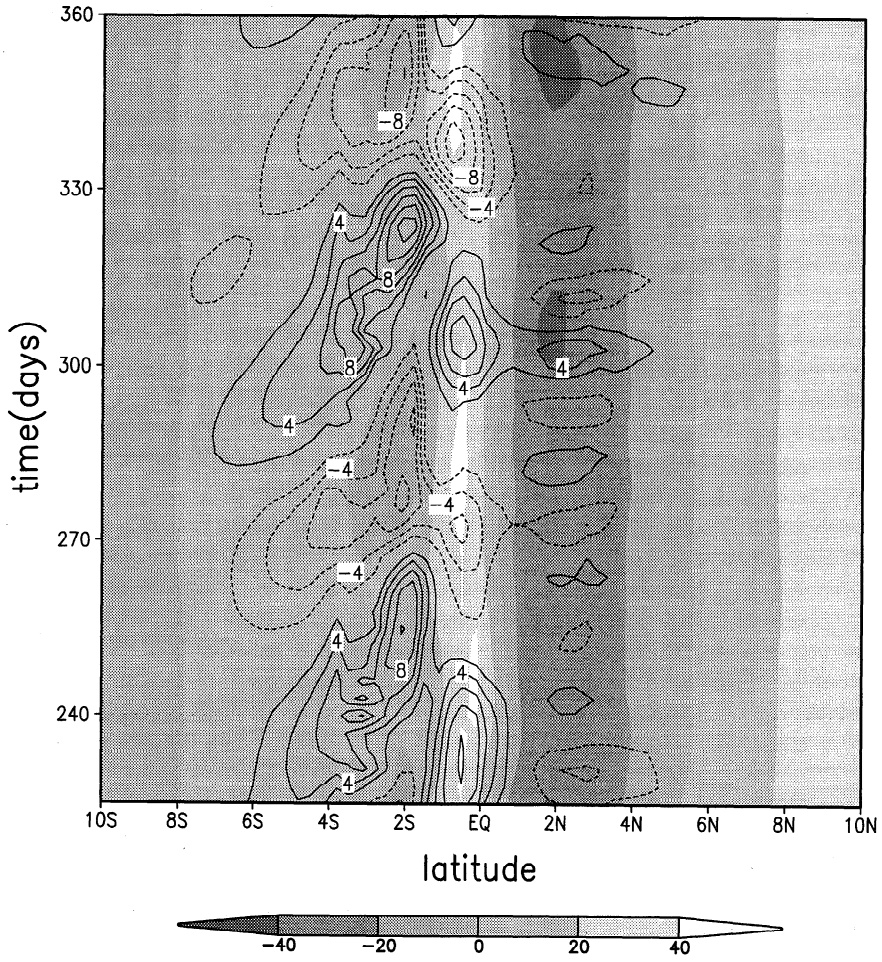

Figure 8. As in Figure 7 but at 95 m. Contour intervals are 20 cm/s for zonal velocity and 2 cm/s for meridional velocity.

the eastern to the western Pacific. The variability in wavelength and period captured by the wavelet analysis shows the response of the waves to changes in the background state.

The field chosen for the analysis is the total meridional velocity, and in particular for the time series, we analyze the meridional velocity during the last 2 years of the model integration at 2°S, at the equator, and at 2°N at various depths and longitudes. The choice of the meridional velocity is justified by the evidence that it is the field with the strongest signal in the tropical instability waves. The first year of integration is not included in the analysis because it is distorted by transient spin-up effects. Moreover, since a distortion of the results occurs within the cones of influence at the beginning and end of the data set, we discard the first 3 and the last 3 months of the temporal data set used for the analysis. The same limitation applies to the meridional velocity data set in the zonal direction, which limits our analysis to those longitudes between 164°E and 126°W. All the plots in sections 4.1 and 4.2 show the modulus of the wavelet coefficients of the signal analyzed.

4.1. Spatial Variability of the Period

The satellite and the in situ data show that the TIWs are intermittent seasonally and interannually and that their period changes from year to year and has a high spatial variability. The numerical simulation that we are going to analyze is performed with fixed wind stress forcing and therefore is not suitable for exploring the temporal variability of the period, but with the wavelet analysis we can examine how the dominant period changes in longitude, latitude, and depth. As all the following plots will demonstrate, there is, nevertheless, a temporal variability in the period of the waves that is due to internal nonlinear dynamics and wave mean flow interaction.

In Figure 10 we show the amplitude of the wavelet coefficient for the meridional velocity at 110°W and 2°N at four different model levels between the surface and 713 m, the region wherein the maxima in the wave signal are confined. As for all the wavelet transform plots to be shown in this section, the vertical axis is the scale dilation parameter that in this case corresponds to the

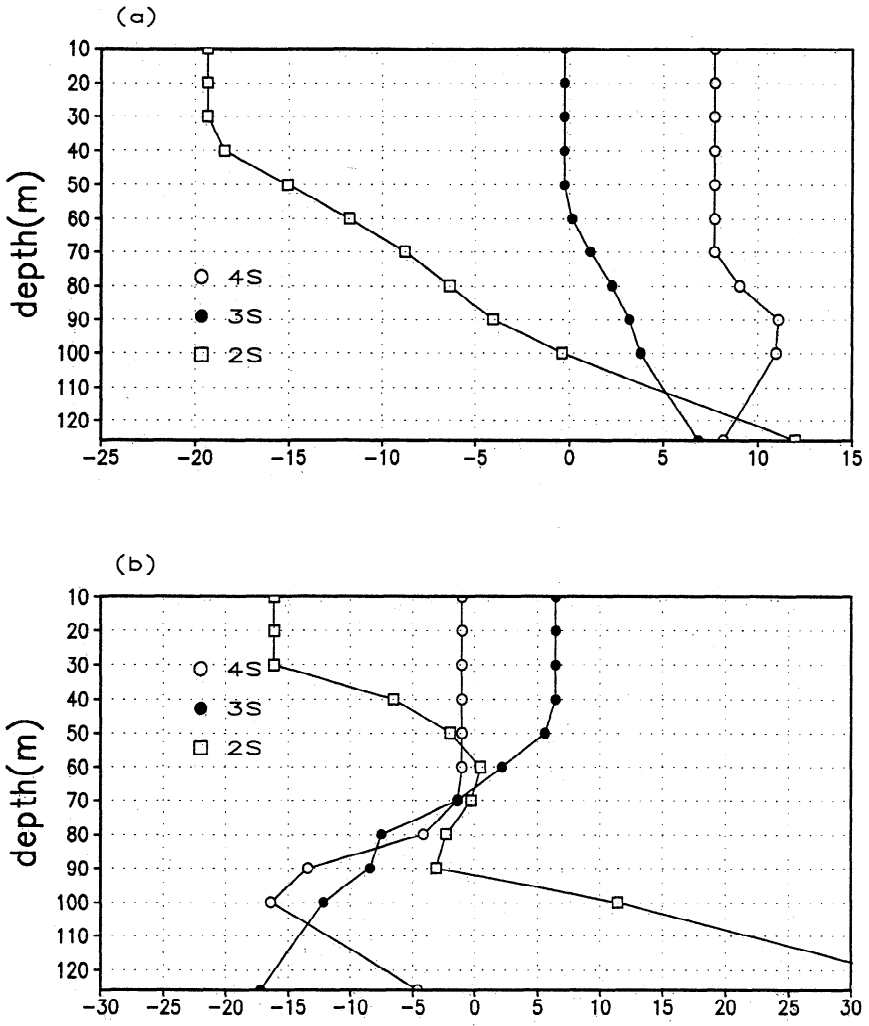

Figure 9. Vertical profiles of (a) time mean zonal velocity (in cm/s) and (b) horizontal convergence of the zonal eddy momentum flux (10^{-7}cm/s^2) at 170°W. In both plots the profiles are taken at 4°S (open circles), 3°S (solid circles), and 2°S (open squares).

period of the signal in days. The horizontal axis represents model time. Regions where the modulus of the wavelet coefficient are heavily shaded indicate a high correlation between the data and the wavelet.

At this location the dominant period delivered from the wavelet transform shows a substantial decrease with depth below 75 m, which represents the mixed layer depth. At the surface and at 75 m the peak in the modulus is between 36 and 39 days, while at 713 m depth the period has been reduced to 24 days. In the thermocline (z=113 m) the two signals are simultaneously present, the faster signal preceding the slower one by $\sim$ 3 months.

In the eastern Pacific and north of the equator the maximum amplitude of the wavelet coefficients has the same value at the surface and at 75 m below the surface. The same occurs at 2°S at the same longitude (not shown), while on the equator the maximum in the wavelet coefficient occurs at the surface as shown in Figure 11. This behavior indicates that the wave signal is confined to the mixed layer, which is particularly shallow at the equator and deepens to $\sim$ 80 m and 120 m a few degrees south and north of the equator, respectively, in the eastern Pacific. This result is in agreement with the energy analysis of the numerical simulation [*Masina et al.*, this issue], which shows a very similar behavior for the kinetic energy.

The wavelet transforms at the equator (Figure 11) and at 2°S are very similar, and at these latitudes the slow (36-39 day) signal at the surface and in the shallower layers is much weaker than at 2°N. The two dominant peaks are between 24 and 27 days and between 27 and 30 days. The maximum at the longer period decays in amplitude with depth and has disappeared completely at 713 m. At the three different latitudes (2°S, 0°, and 2°N) both signals do not show any phase shift from the surface down to the thermocline, but below the thermocline the maxima are shifted in such a way to lead the upper level maxima during the first half of the analysis period and to lag the upper level max-

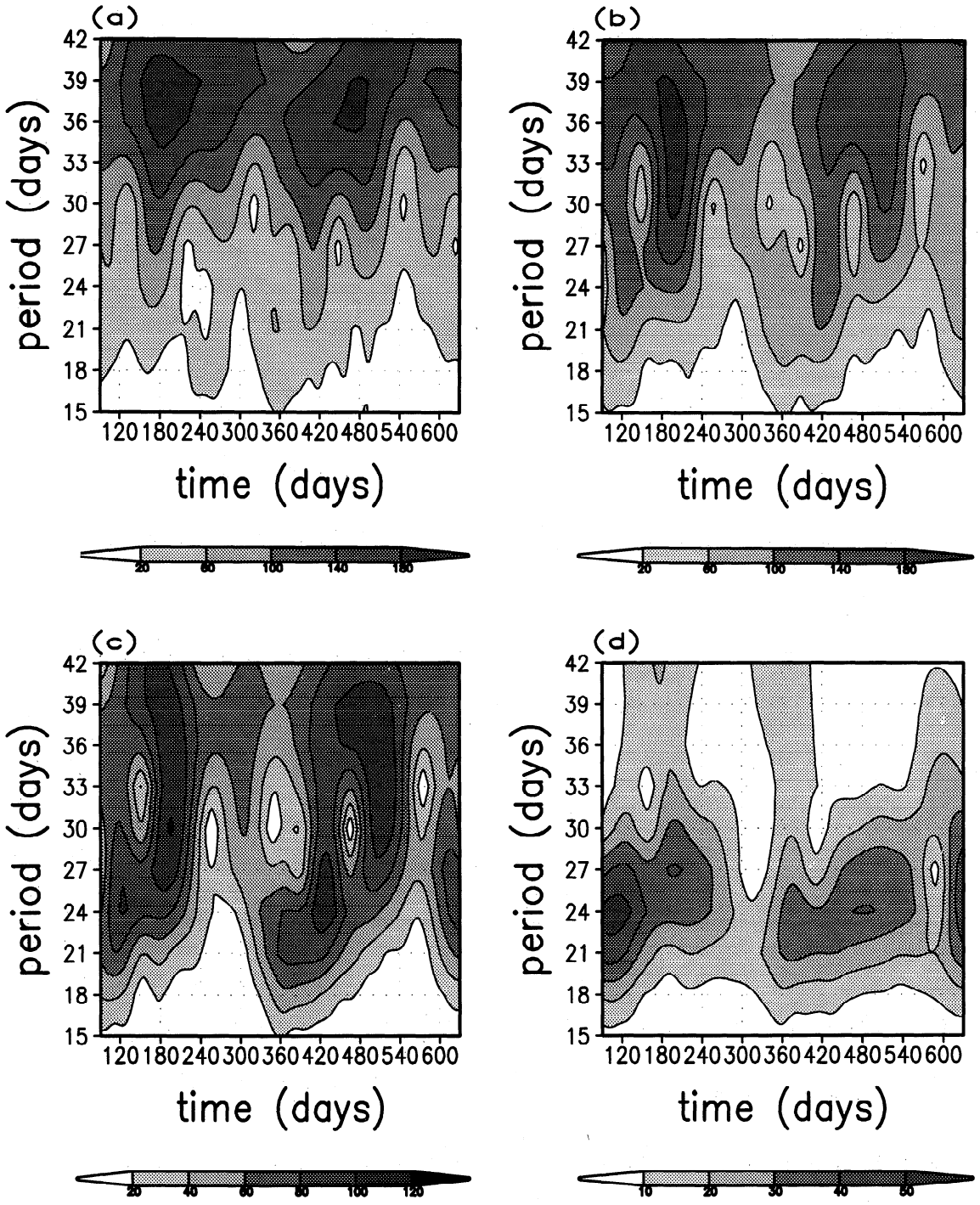

Figure 10. Modulus of the wavelet transform coefficients of meridional velocity at 110°W and 2°N at (a) 5 m, (b) 75 m, (c) 113 m, and (d) 713 m. Time is on the x axis and period (in days) is on the y axis. The CI (in cm/s) is indicated by the color bar under each plot.

ima during the second half. At 713 m the amplitude of the wavelet transform is only 30% of the amplitude in the mixed layer, which verifies that the TIW signal is confined to the upper ocean above the base of the thermocline. At 140°W and 2°N, (Figure 12) the amplitude reduction of the signal below the thermocline (at $\simeq$ 180 m) is even more evident, being only 7% of the surface signal. The maximum corresponds to a period of 21 days at all depths from the surface down to the bottom of the mixed layer at 113 m, while at 713 m the dominant period is around 24 days with a secondary maximum around 42 days (although these peaks are very weak). The 42 day maximum at 713 m is also present at 2°S and is particularly evident at 4°N (not shown), while it is completely absent at the equator. This mode does not seem to be related to a TIW and is more likely a Rossby wave propagating at a higher latitude. The signal does not show any phase shift from

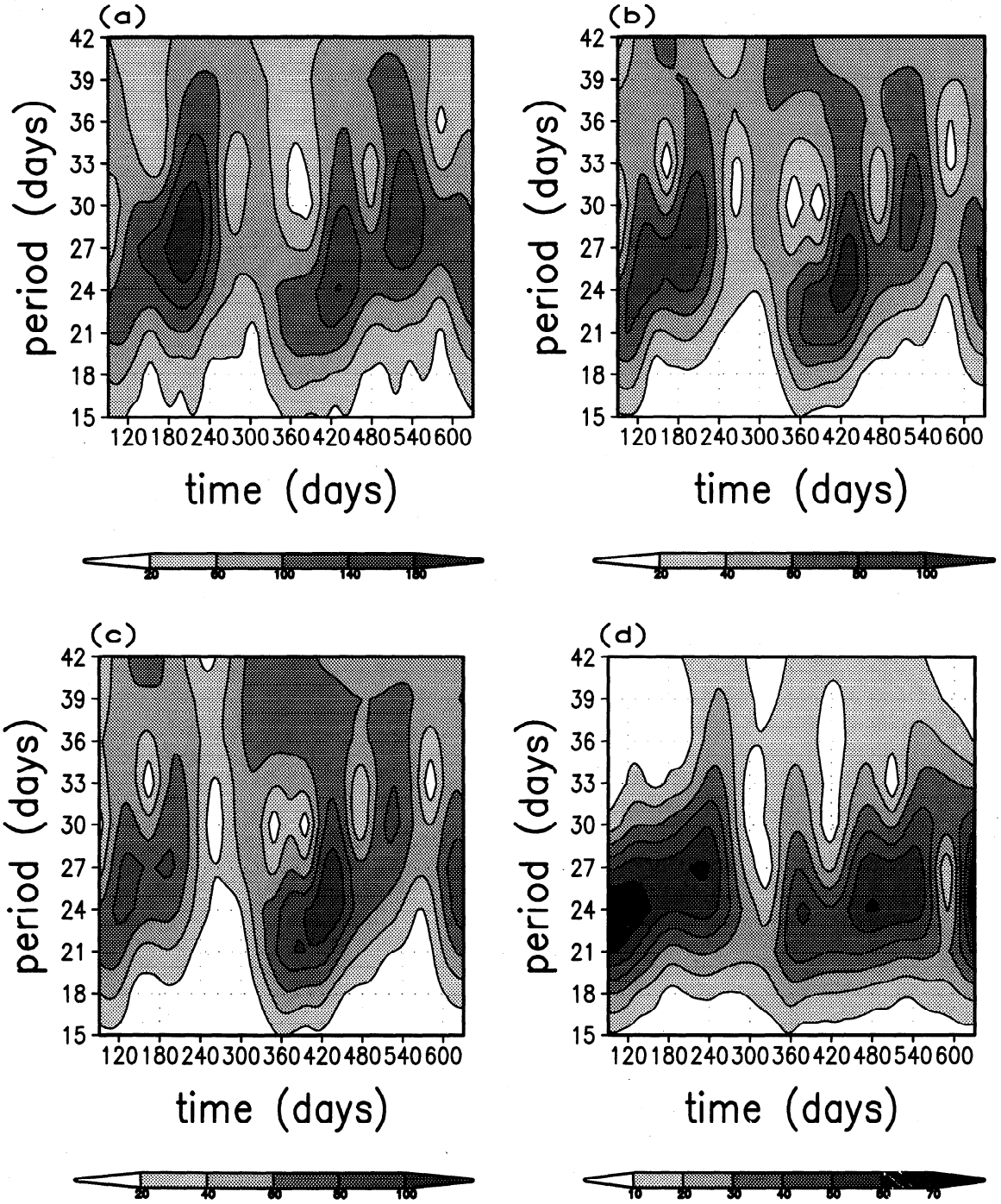

Figure 11. Same as in Figure 10 but at 110°W and the equator.

the surface down to 113 m at all latitudes but is phase shifted in latitude going from 2°N to the equator with the northward signal preceding the equatorial one by ~ 2 months. We did not find any meridional phase shift at 110°W.

The wavelet analysis at 170°W reveals the abrupt change in phase speed between the eastern and the western Pacific south of the equator (see section 3). At 2°N (not shown) the dominant period is between 21 and 24 days from the surface down to 113 m, as was the case in the eastern longitudes. At the equator (not shown) a 21-24 day peak is also dominant at 75 m. Figure 13 shows the wavelet transform at 2°S and 170°W. Note that we necessarily changed the scale of the vertical axis in order to include the maxima that at this location, are centered mainly around a 69-72 day period from the surface down to 113 m. In Figure 13 we show only a portion of the time period examined in the previous wavelet analyses in order to eliminate all the results that fall inside the cone of influence. The latter is necessarily larger in this case since we analyze larger periods. Below the thermocline (at $\simeq$ 200 m) the dominant signal

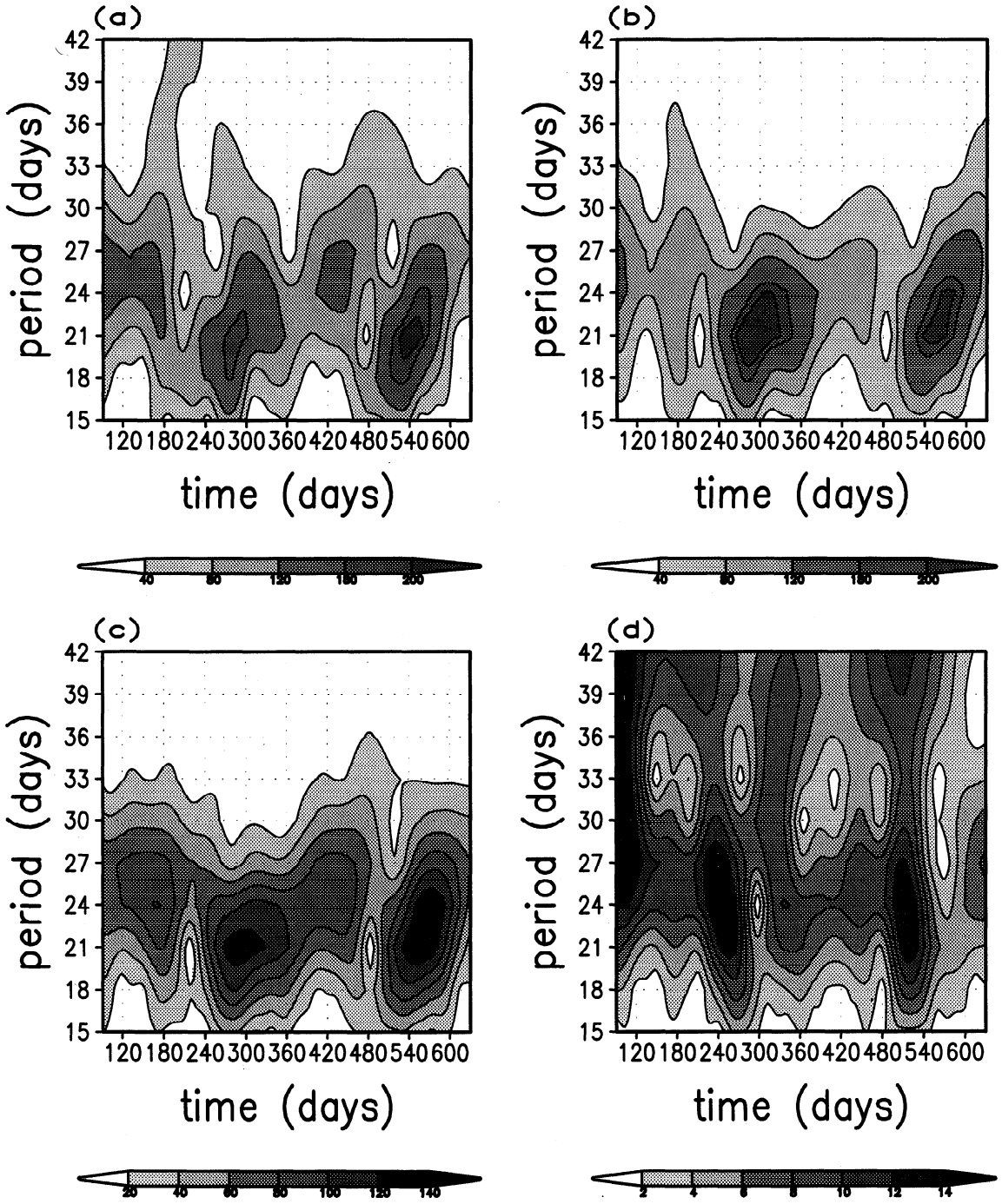

Figure 12. Same as in Figure 10 but at 140°W and 2°N.

has a 60-63 day period with an amplitude that decreases in time. The lower frequency signal (69-72 day) inside and above the thermocline is present only during the second year of the numerical integration, which suggests that these waves have a slower growth rate with respect to the higher frequency instability waves that develop in the eastern Pacific. The amplitude of the signal at 75 and 113 m is twice the amplitude of the surface signal, suggesting that the waves in the western Pacific grow and develop preferentially below the surface.

4.2. Spatial Variability of the Wavelength

The wavelet method allows us to unfold a space-dependent signal $f(x)$ into both space and wavenumber domains. At a time close to the end of the numerical integration and at a fixed latitude and depth, we perform the wavelet analysis of the meridional velocity as a function of longitude to determine if and how the wavelength of the TIW changes inside the model domain.

Figure 14 shows the amplitude of the wavelet coefficient at 2°N and 2°S as a function of longitude and

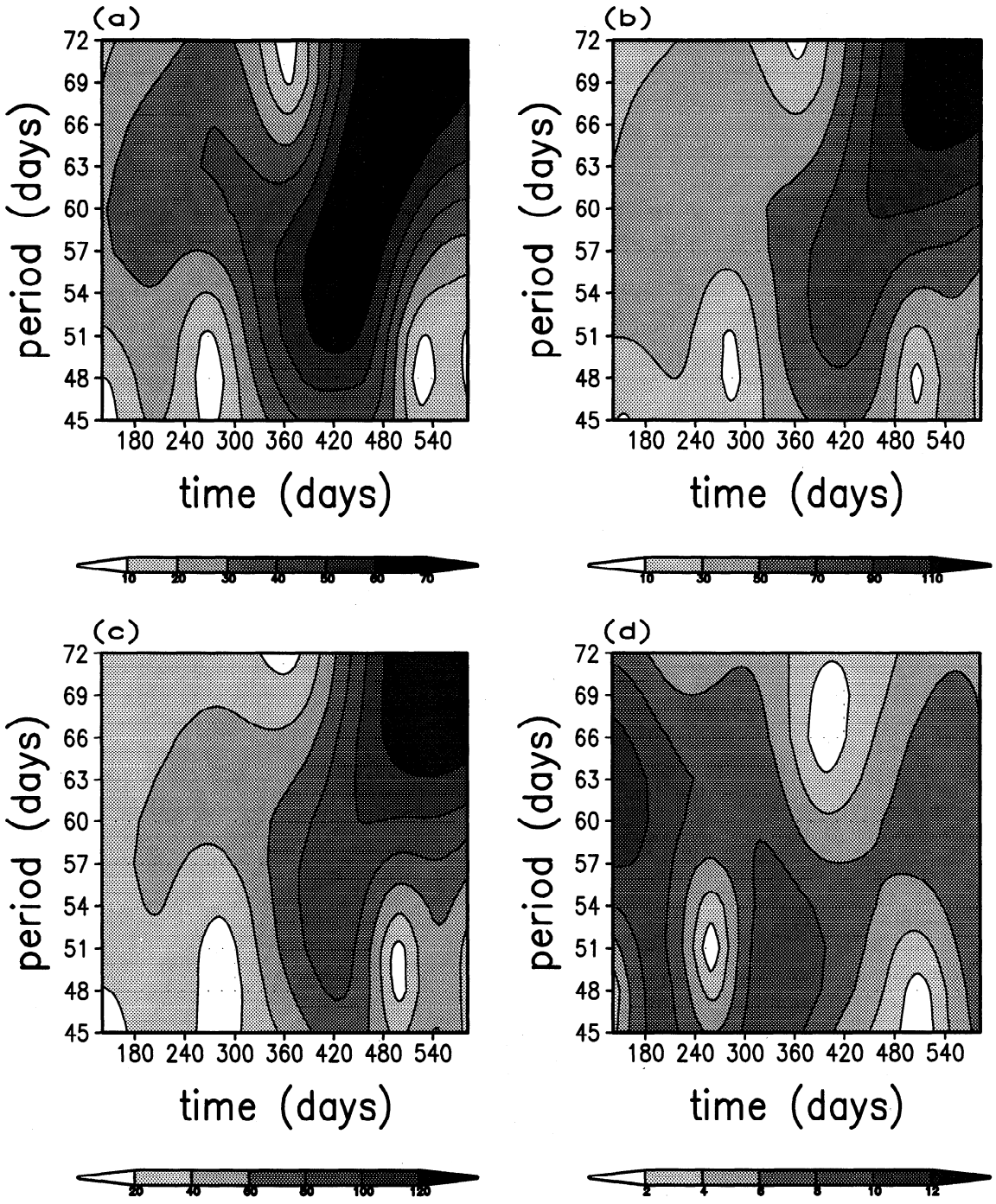

Figure 13. Same as in Figure 10 but at 170°W and 2°S.

wavelength (in km) at two depths (5 and 713 m at 2°N and 5 and 113 m at 2°S). The wavelengths on the vertical axes have been obtained through a proper scaling of the so-called dilation parameter.

In Figure 14a the wavelet analysis of the surface signal demonstrates that the dominant wavelength of the TIW is centered near 800 km in the eastern Pacific Ocean. Considering that at the surface, at 140°W and 2°N, the dominant period is 21 days, this implies a phase speed of approximately -48 cm/s in the region where the waves are generated. This value is in good agreement with the value of the phase speed of TIWs found in observations. In the central and western Pacific the wave signal is so weak with respect to the eastern signal that the convolution between the mother wavelet and the signal itself cannot capture any particular wavelength. Below the thermocline, at z=713 m (Figure 14b); the dominant wavelength is longer than at the surface at all longitudes, and in particular, it reaches a maximum length of 1200 km east of 140°W.

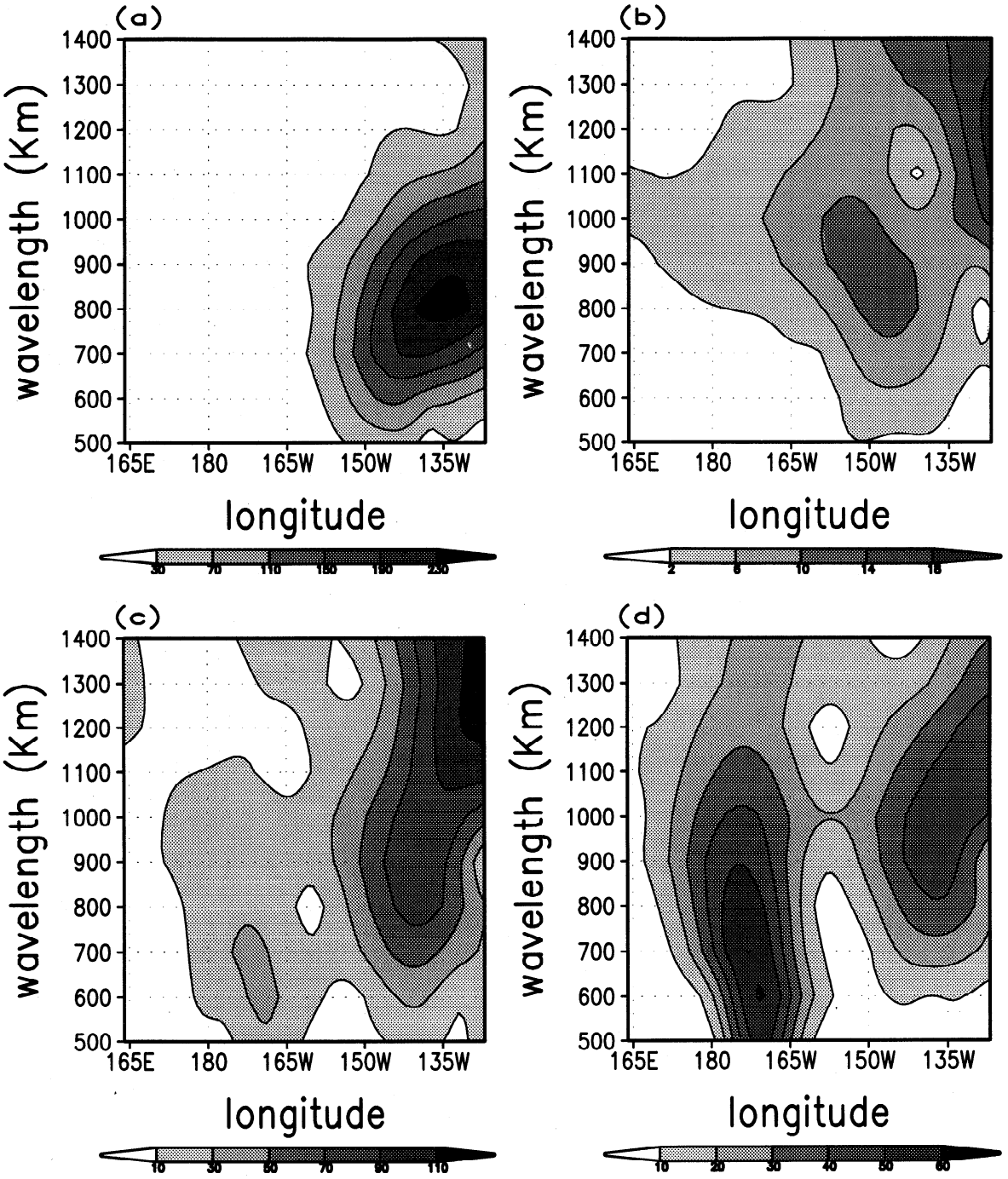

Figure 14. Modulus of the wavelet transform coefficients of meridional velocity at t=180 and at 2°N at (a) 5 and (b) 713 m and at 2°S at (c) 5 and (d) 113 m. Longitude is on the x axis and wavelength (in km) is on the y axis. The CI (in cm/s) is indicated by the color bar under each plot.

Another secondary maximum corresponding to a wavelength of 900 km is centered at 150°W. The comparison between the wavelet analysis of the wavelength at the surface (Figure 14a) and below the thermocline (Figure 14b) supports the hypothesis that part of the wave energy generated at the surface near 135°W propagates downward and splits into one westward and one eastward propagating signal. This subsurface signal may indeed be of neutral equatorial waves that have been excited by the surface instability and that are propagating downward [e.g., *Weisberg et al.*, 1979]. At 713 m the dominant period is 24 days at both 110° and 140°W, giving phase speeds of -64 and -48 cm/s at the two longitudes, respectively.

The analysis on the equator (not shown) gives approximately the same results both in terms of values and of spatial variability of the wavelength. At all the levels above the thermocline the wavelength does not

present any remarkable change in longitude in the region where the wave signal is stronger (130°-150°W).

South of the equator the situation is significantly different. At the surface, there is a distinct separation between the eastern and the central regions as is clearly shown in Figure 14c. In the far eastern part of the domain the maximum in the wavelet coefficient amplitude is around 1300-1400 km and decreases to 900 km around 140°W. At 170°W, there is another distinct peak in the wavelet coefficient amplitude, and the dominant wavelength has a value of 600-700 km. This region south of the equator between 160° and 180°W is the anomaly region where the waves show a considerable change in their dominant period, which according to the results obtained in section 4.1, is 70 days. This gives a phase speed of -11 cm/s for the instabilities at this location. The amplitude of the wavelet transform shows that at the surface the wave signal in the eastern Pacific is the dominant one, while in the thermocline, at z=113 m (see Figure 14d), the central wave signal prevails over the signal in the eastern Pacific. This confirms the hypothesis that the southcentral instability is generated below the surface while the north instability seems to be excited closer to the surface.

The results from several idealized numerical simulations performed in a channel model centered on the equator and initialized with zonally uniform jets resembling the SEC and the EUC [*Masina,* 1996] are extremely helpful in interpreting more complex results obtained from the wind-forced simulation of the Pacific Ocean. In particular, the channel experiments reveal clearly the drastic difference in phase speed between the waves that develop in the eastern Pacific and those generated in the central Pacific south of the equator. The stability analysis of the periodic channel simulations [*Masina,* 1996] has shown that the dispersion characteristics of the unstable waves depend on the direction of the mean flow and its associated temperature structure. In particular, the simulations in the channel model showed that a subsurface eastward jet centered on the equator and with speed comparable to the EUC velocity generates unstable disturbances that can propagate either eastward or westward, depending on the thermal structure of the flow, with a phase speed much slower than the phase speed of the unstable waves which grow in surface westward jets resembling the SEC. The wave dispersion characteristics obtained in the experiments initialized with subsurface eastward jets are in good agreement with the properties of the low-frequency waves generated in the central Pacific in the wind-forced numerical simulation. These waves are $\simeq$ 4 times slower than those that arise in the eastern Pacific. Here the waves have a phase speed comparable with the phase speed of the waves generated in a channel model and initialized with surface westward jets with speed comparable to the SEC velocity. If we consider that in the central Pacific the low-frequency waves south of the equator reach their maximum amplitude below the surface at a depth of 100 m, while in the eastern Pacific the amplitude of the waves is maximum at the surface, we can conclude that the instabilities that grow in the central Pacific are generated in the EUC region, while in the eastern Pacific the unstable waves grow in the SEC. This explains the drastic difference between their phase speeds as demonstrated by the experiments in the channel model [*Masina,* 1996].

5. Summary and Conclusions

A multilevel general circulation model configured for the equatorial Pacific and forced by August 1988 conditions representing an extraordinarily strong La Niña year is able to reproduce TIWs with characteristics that are very similar to the waves detected in observations. The unstable waves develop with preference north of the equator in the eastern Pacific between 120° and 140°W. Some eddies also grow south of the equator, and they are confined in a 2° latitudinal band near the equator, while the meridional extent of the northern instabilities is larger. In particular, the oscillations extend up to 4° and 6°N in the experiments with weak and strong winds, respectively. The amplitude of the instabilities is not largely affected by the strength of the zonal wind stress. On the contrary, the wind stress acts to enhance the westward propagation of the waves considerably. In the experiment with stronger winds the oscillations propagate to the west beyond the date line, confirming some measurements [*Halpern,* 1989; *Kuroda and McPhaden,* 1993] which reported a TIW signal in the western Pacific. South of the equator, between 160° and 180°W, the unstable oscillations show a dramatic decrease in their phase speed, especially in the experiment with weaker wind.

The mean flow at 130°W in the generation region of the instabilities shows that the strongest meridional shears occur between the EUC and the northern branch of the SEC at around 1°N and in the EUC itself at around 2°S. At these latitudes the latitudinal gradient of the potential vorticity changes sign, indicating that these regions are potentially barotropically unstable. The shear between the SEC and the NECC is much weaker and does not seem to be involved in the generation process of the TIWs as was also found by *Yu et al.,* [1995]. However, it is necessary to point out that the NECC simulated by our model appears to be weaker than the observed NECC during the summer of 1988 [*McPhaden,* 1996]. The maximum meridional temperature gradient is found between 4° and 6°N, suggesting that this region might be baroclinically unstable. The instabilities generated in the eastern Pacific consist of two components phase locked to each other. One component develops between 2°S and the equator and the other between 2° and 4°N. No decoupled modes have been observed in the eastern Pacific in our nu-

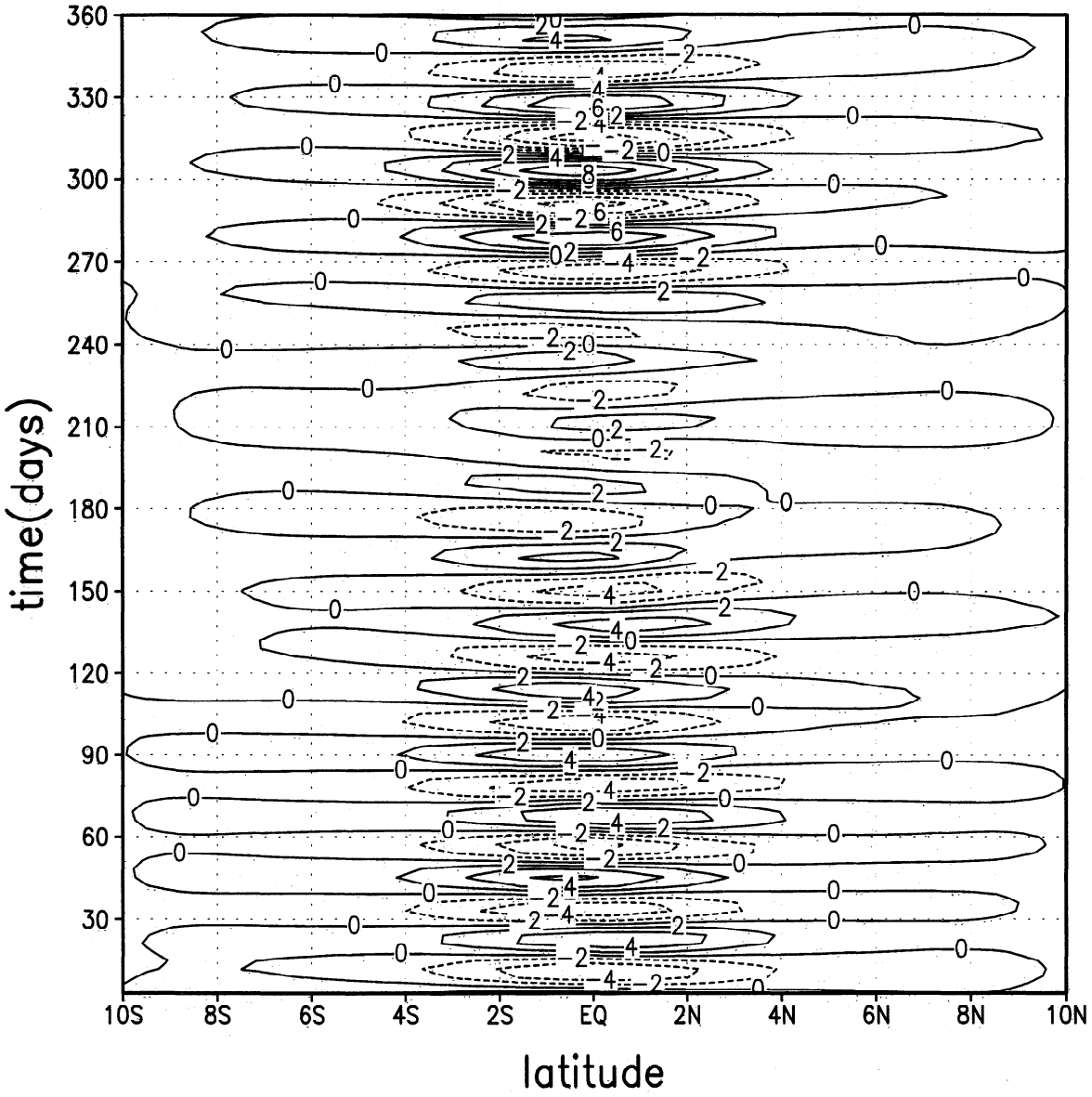

Figure 15. Time-latitude diagram of perturbation meridional velocity at 110°W and z=2575 m. CI is 2 cm/s.

merical simulations. The regions where the instabilities grow are characterized by strong latitudinal shears of the mean flow and of the temperature.

The wavelet transform technique is applied to the three-dimensional field obtained from the wind-forced numerical simulation. This method provides a detailed analysis of the spatial variability of the period and the wavelength of the TIWs in the domain of integration. At 140°W and 2°N, i.e., the generation region of the TIWs in the eastern Pacific, the dominant period is 21 days from the surface down to the bottom of the mixed layer, and it increases to 24 days in the thermocline where another maximum, peaked around 42 days, appears. This result demonstrates that the period of the instability waves becomes larger below the surface, a result that has substantial observational support [*Philander et al.*, 1985; *McPhaden and Taft*, 1988]. The period also increases with latitude away from the equator. At 140°W and 7°N the dominant period is 24 days, but there is also evidence of a slower and weaker signal ($\simeq$ 36 days) present from the surface down to the thermocline. This result is also in agreement with observations [*Philander et al.*, 1985]. East of the generation region and north of the equator the wavelet analysis shows an opposite tendency with larger periods at the surface that decrease going downward. North of the equator in the mixed layer the dominant period decreases from 36 to 21 days going from 110° to 140°W. The decreasing tendency of the period of the oscillations moving westward is in agreement with measurements [*Halpern et al.*, 1988]. The dominant wavelength is centered at 800 km in the eastern domain at the surface, and this gives a

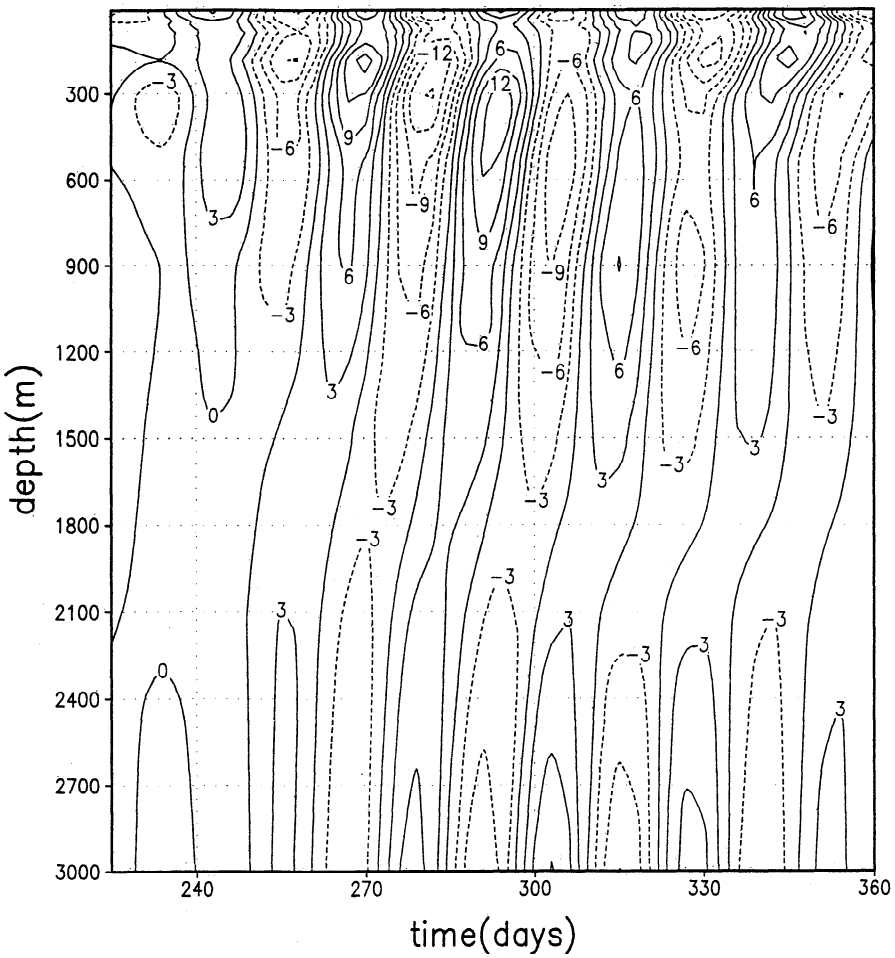

Figure 16. Depth-time diagram of perturbation meridional velocity at 110°W and the equator. CI is 3 cm/s.

phase speed of -48 cm/s. Below the thermocline the wavelet analysis shows two dominant wavelengths: at 1200 and 900 km east and west of 140°W, respectively. The splitting of the maximum confined to the thermocline into two signals below the thermocline located at the east and the west of the surface signal supports the evidence that part of the wave energy generated at the surface propagates downward through one eastward and one westward neutral waves. In particular, the analysis of the numerical experiments shows evidence of a mixed Rossby-gravity mode that propagates downward and to the east, while a first meridional mode Rossby wave is present west of the date line below the thermocline and propagates westward. Figure 15, which shows the perturbation meridional velocity at 110°W at the last model level, clearly demonstrates that a mixed Rossby-gravity mode is present in this experiment. This deep mode might be excited from the unstable oscillations that are confined to the upper ocean and is the only mode present at this longitude below 300 m. This latter point is made more evident from a vertical section of the perturbation meridional velocity at the equator (Figure 16). The unstable oscillations are confined to the mixed layer (< 100 m) but, nevertheless, seem to excite a signal that propagates below the surface with a downward group velocity of $\simeq 2 \times 10^{-2}$ cm/s. At this longitude the perturbation signal is present at the bottom of the domain but is not constant with depth. The perturbation decays vertically down to $\sim$ 1800 m; thereafter it increases in amplitude toward the bottom in a pattern that suggests reflective interference. Figure 16 also reveals that below the mixed layer the phase velocity is upward.

Near the bottom of the domain at 130°W (not shown) the time-latitude plot of the perturbation velocity looks very different than at 110°W. At this longitude, there is no evidence of the mixed Rossby-gravity mode that was so prominent at 110°W.

The oscillations analyzed in the eastern Pacific contain many features of equatorially trapped mixed Rossby-gravity waves, such as westward and upward propagation of phase and eastward and downward propagation of energy. Although the data showed evidence mainly of this wave [*Weisberg et al.*, 1979; *Weisberg and Horigan*, 1981], downward and westward first meridional mode Rossby waves have also been observed

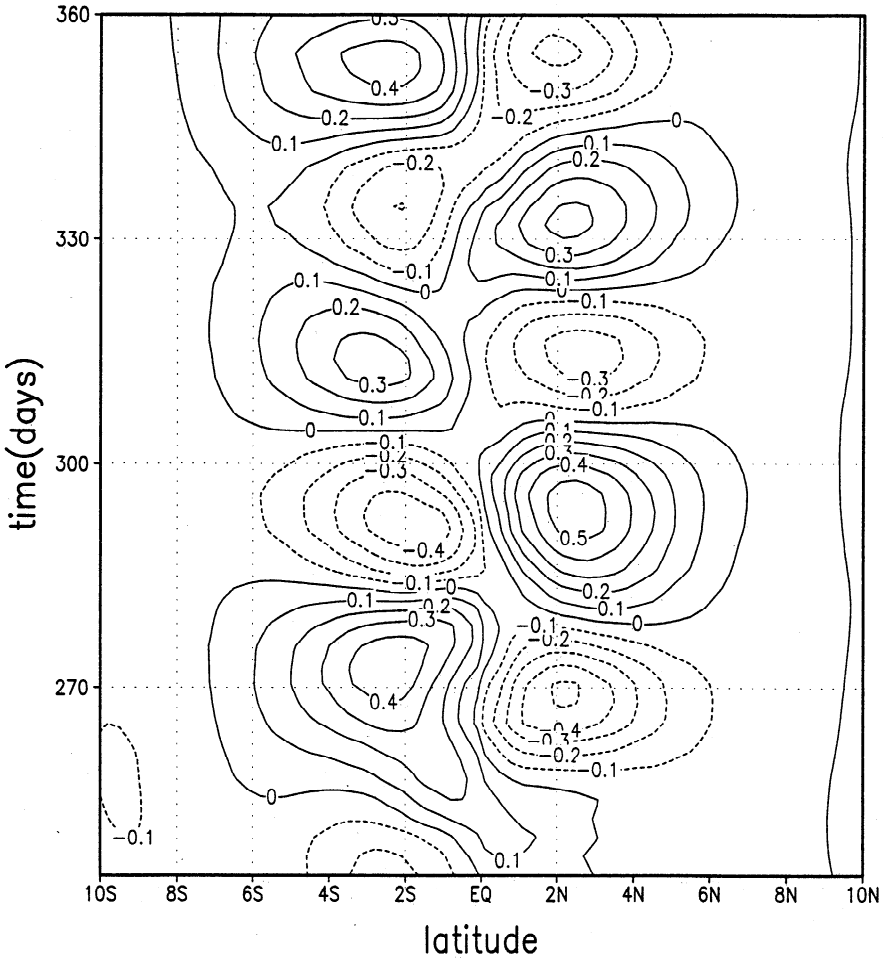

Figure 17. Time-latitude section of perturbation meridional velocity at 170°E at a depth of 713 m. Contour interval is 0.1 cm/s.

[*Eriksen and Richman,* 1988], and *Philander* [1979] showed that a Rossby-gravity wave propagating downward through the EUC can excite a Rossby-gravity mode plus several Rossby modes, each with different latitudinal structure, in the deep ocean. Our simulations give additional indication for the presence of pure Rossby waves: west of the date line at 170°E, below the thermocline, a pure m=1 Rossby wave (where m is the meridional number) is clearly visible in V', as shown in Figure 17. This wave has a westward group velocity and may explain why a considerable amount of energy is found to the west of the generation area of the TIWs. Both these kinds of waves, Rossby and Rossby-gravity, provide a mechanism by which eddy energy generated near the surface can be transported to the deep water, and we have demonstrated the presence of both in our simulations, although their three-dimensional spatial structure is extremely complex. The availability of equatorial neutral waves radiating from the surface down to the bottom of the ocean is peculiar to the equatorial wave guide region, and it might explain why the instability waves in the Pacific Ocean never become sufficiently nonlinear to break [*Philander,* 1978b, 1979].

In summary, the wavelet analysis shows that the instabilities in the eastern Pacific are confined to the mixed layer; that is, they are particularly shallow at the equator and deepen north and south of the equator. In the eastern Pacific the phase speed of the simulated TIWs varies in a range between -48 and -72 cm/s. These values are in good agreement with the phase speeds inferred from observations [*Qiao and Weisberg,* 1995; *Kuroda and McPhaden,* 1993]. The instabilities in the central Pacific south of the equator show the largest amplitude below the surface at the base of the mixed layer. These instabilities appear only during the second year of the numerical integration and have a dominant period of 70 days. This means that these instabilities not only have a much lower frequency with respect to the oscillations in the eastern Pacific but also have a slower growth rate. The dominant wavelength in the western Pacific south of the equator is 600-700 km, giving a phase speed of approximately -11 cm/s.

Finally, the spatial nonhomogeneity of the TIWs is manifested through a high variability in both their period and their wavelength. The dispersion characteristics of the instabilities change with latitude and longitude, as well as with depth. In particular, the drastic change in longitude of the phase speed of the instabilities generated in the wind-forced simulations can be interpreted through the results obtained from the exper-

iments performed with a periodic channel model initialized with zonally uniform jets and resembling different idealized equatorial mean flows [*Masina* 1996].

Acknowledgments. We would like to thank A. Bush and D. Gu for their helpful discussions and advice. This work was supported by the Department of Commerce/ NOAA grant NA56GP0026. One of the authors (SM) was partially supported by a NASA Global Change Fellowship NGT-30288. We also thank two anonymous reviewers for their helpful comments.

References

Bryan, K., and M.D. Cox, A numerical investigation of the ocean general circulation, *Tellus, 19,* 54-80, 1967.

Combes, J.M., A. Grossmann, and P. Tchamitchian, *Wavelets: Time-Frequency Methods and Phase Space,* 315 pp., *Springer-Verlag,* New York, 1989.

Cox, M.D., Generation and propagation of 30-day waves in a numerical model of the Pacific, *J. Phys. Oceanogr., 10,* 1168-1186, 1980.

Cox, M.D., A primitive equation, 3-dimensional model of the ocean, *Ocean Group Tech. Rep. 1,* 143 pp., Geophys. Fluid Dyn. Lab., Princeton, N.J., 1984.

Eriksen, C.C., and J.G. Richman, An estimate of equatorial wave energy flux at 9- to 90-day periods in the central Pacific, *J. Geophys. Res., 93,* 15,455-15,466, 1988.

Farge, M., Wavelet transform and their application to turbulence, *Ann. Rev. Fluid Mech., 24,* 395-457, 1992.

Halpern, D., Detection of 17.5-day period meridional current oscillations in the equatorial western Pacific Ocean during 1985, *Geophys. Res. Lett., 16,* 499-502, 1989.

Halpern, D., R.A. Knox, and D.S. Luther, Observations of 20-day period meridional current oscillations in the upper ocean along the Pacific equator, *J. Phys. Oceanogr., 18,* 1514-1534, 1988.

Kuroda, Y., and M.J. McPhaden, Variability in the western equatorial Pacific Ocean during japanese Pacific climate study cruises in 1989 and 1990, *J. Geophys. Res., 98,* 4747-4759, 1993.

Legeckis, R., Long waves in the eastern equatorial Pacific Ocean: A view from a geostationary satellite, *Science, 197,* 1179-1181, 1977.

Levitus, S., Climatological atlas of the world ocean, *NOAA Prof. Pap. 13,* U.S. Govt. Print. Office, Washington D. C., 1982.

Masina, S., Tropical instability waves in the Pacific Ocean, Ph.D. thesis, 242 pp., Princeton Univ., Princeton, N. J., 1996.

Masina, S., S.G.H. Philander, and A.B.G. Bush, An analysis of tropical instability waves in a numerical model of the Pacific Ocean, 2, Generation and energetics of the waves, *J. Geophys. Res.,* this issue.

McCreary, J.P., Jr, and Z. Yu, Equatorial dynamics in a $2\frac{1}{2}$-layer model, *Prog. Oceanogr., 29,* 61-132, 1992.

McPhaden, M.J., Monthly period oscillations in the Pacific North Equatorial Countercurrent, *J. Geophys. Res., 101,* 6337-6359, 1996.

McPhaden, M.J., and B.A. Taft, Dynamics of seasonal and intraseasonal variability in the eastern equatorial Pacific, *J. Phys. Oceanogr., 18,* 1713-1732, 1988.

Meyers, S.D., B.G. Kelly, and J.J. O'Brien, An introduction to wavelet analysis in oceanography and meteorology: With application to dispersion of Yanai waves, *Mon. Weather Rev., 121,* 2858-2866, 1993.

Orlanski I., Localized baroclinicity: A source for meso-α cyclones, *J. Atmos. Sci., 43,* 2857-2885, 1986.

Orlanski I., and M.D. Cox, Baroclinic instability in ocean currents, *Geophys. Fluid Dy., 4,* 297-332, 1973.

Pacanowski, R.C., Effect of equatorial currents on surface stress, *J. Phys. Oceanogr., 11,* 1443-1451, 1987.

Pacanowski, R.C., and S.G.H. Philander, Parameterization of vertical mixing in numerical models of tropical oceans, *J. Phys. Oceanogr., 11,* 1443-1451, 1981.

Pacanowski, R., K. Dixon, and A. Rosati, The G.F.D.L. modular ocean model users guide, *Ocean Group Tech. Rep. 2,* 1993.

Philander, S.G.H., Instabilities of zonal equatorial currents, *J. Geophys. Res., 81,* 3725-3735, 1976.

Philander, S.G.H., Instabilities of zonal equatorial currents, 2, *J. Geophys. Res., 83,* 3679-3682, 1978a.

Philander, S.G.H., Forced oceanic waves, *Rev. Geophys., 16,* 15-46, 1978b.

Philander, S.G.H., Equatorial waves in the presence of the equatorial undercurrent, *J. Phys. Oceanogr., 9,* 254-262, 1979.

Philander, S.G.H., and R.C. Pacanowski, A model of the seasonal cycle in the tropical Atlantic Ocean, *J. Geophys. Res., 91,* 14,192-14,206, 1986.

Philander, S.G.H., D. Halpern, D. Hansen, R. Legeckis, L.Miller, C. Paul, R. Watts, R. Weisberg, and M. Wimbush, Long waves in the equatorial Pacific Ocean, *Eos Trans. AGU, 66,* 14, 154-156, 1985.

Philander, S.G.H., W.J. Hurlin, and R.C. Pacanowski, Properties of long equatorial waves in models of the seasonal cycle in the tropical Atlantic and Pacific Oceans, *J. Geophys. Res., 91,* 14,207-14,211, 1986.

Philander, S.G.H., W.J. Hurlin and R.C. Pacanowski, Initial condition for a general circulation model of tropical oceans, *J. Phys. Oceanogr., 17,* 147-157, 1987.

Proehl, J.A., Linear stability of equatorial flows, *J. Phys. Oceanogr., 26,* 601-621, 1996.

Qiao, L., and R.H. Weisberg, Tropical instability wave kinematics: Observations from the Tropical Instability Wave Experiment, *J. Geophys. Res., 100,* 8677-8693, 1995.

Rioul, O., and M. Vetterli, Wavelets and signal processing, *IEEE Signal Process. Mag.,* 14-38, 1991.

Schopf, P.S., and M.A. Cane, On equatorial dynamics, mixed layer physics and sea surface temperature, *J. Phys. Oceanogr., 13,* 917-935, 1983.

Seigel, A.D., A comment on long waves in the Pacific Ocean, *J. Phys. Oceanogr., 15,* 1881-1883, 1985.

Semtner, A.J., Jr, and W.R. Holland, Numerical simulation of equatorial ocean circulation, I, A basic case in turbulent equilibrium, *J. Phys. Oceanogr., 10,* 667-693, 1980.

Weisberg, R.H., Equatorial waves during GATE and their relation to the mean zonal circulation, *Deep Sea Res. Part A, 26,* suppl. 2, 179-198, 1979.

Weisberg, R.H., and A.M. Horigan, Low-frequency variability in the equatorial Atlantic, *J. Phys. Oceanogr., 11,* 913-920, 1981.

Weisberg, R.H., A. Horigan, and C. Colin, Equatorially trapped Rossby-gravity wave propagation in the Gulf of Guinea, *J. Mar. Res., 37,* 67-86, 1979.

Yu, Z., J.P. McCreary Jr., and J.A. Proehl, Meridional asymmetry and energetics of tropical instability waves, *J. Phys. Oceanogr., 25,* 2997-3007, 1995.

S. Masina, ISAO, CNR, Via Gobetti, 101, 40129 Bologna, Italy. (s.masina@isao.bo.cnr.it)

S.G.H. Philander, Atmospheric and Oceanic Sciences Program, Princeton University, Princeton, N.J., 08544. (gphlder@splash.Princeton.EDU)

(Received November 12, 1997; revised April 12, 1999; accepted July 28, 1999.)